Structure

Article

Unique mechanisms to increase structural stability and enhance antigen binding in nanobodies

Graphical abstract

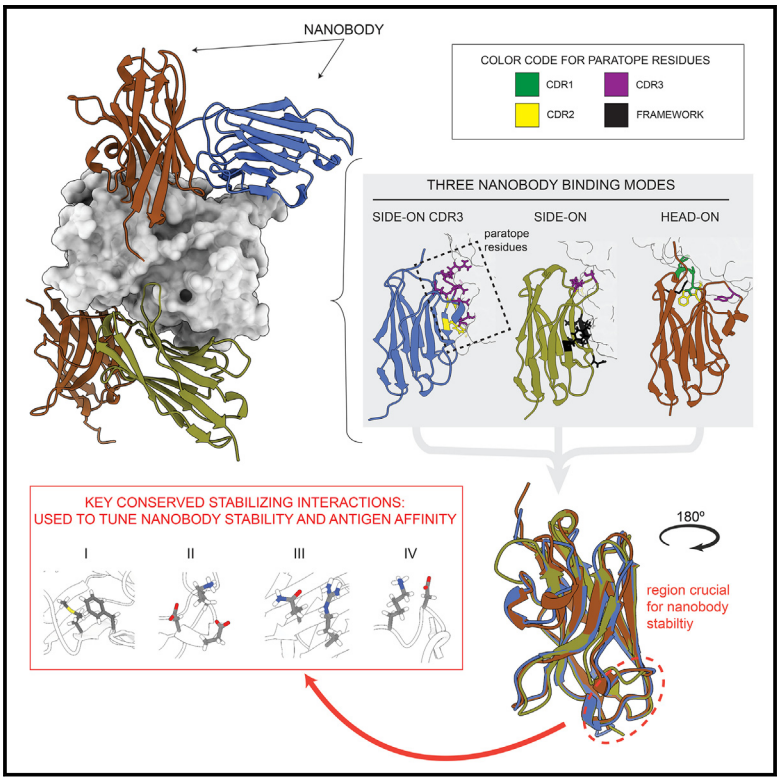

Highlights

- Nanobodies bind their antigen in one of three orientations determined by their paratope
- A highly conserved region within nanobody framework 3 is critical for nanobody stability
- Nanobody stability directly influences antigen affinity
- A universal strategy to tune nanobody stability via a single framework 3 point mutation

Authors

Natalia E. Ketaren, Peter C. Fridy, Vladimir Malashkevich, ..., Steven C. Almo, Brian T. Chait, Michael P. Rout

Correspondence

nketaren@rockefeller.edu (N.E.K.), rout@rockefeller.edu (M.P.R.)

In brief

This study integrates structural, biochemical, and biophysical analyses to reveal that a nanobody's antigen-binding affinity is linked to its stability, and furthermore identifies a conserved region within the nanobody scaffold that can be reengineered to enhance stability – revealing key insights into the interplay between nanobody structure and function.

Ketaren et al., 2025, Structure *33*, 1–14
April 3, 2025
https://doi.org/10.1016/j.str.2025.01.019

CellPress

Please cite this article in press as: Ketaren et al., Unique mechanisms to increase structural stability and enhance antigen binding in nanobodies, Structure (2025), https://doi.org/10.1016/j.str.2025.01.019

Structure

CellPress

Article

Unique mechanisms to increase structural stability and enhance antigen binding in nanobodies

Natalia E. Ketaren,[1,*] Peter C. Fridy,[1] Vladimir Malashkevich,[2] Tanmoy Sanyal,[3] Marc Brillantes,[1] Mary K. Thompson,[1] Deena A. Oren,[4] Jeffrey B. Bonanno,[2] Andrej Šali,[3] Steven C. Almo,[2] Brian T. Chait,[5] and Michael P. Rout[1,6,7,*]

[1]Laboratory of Cellular and Structural Biology, The Rockefeller University, New York, NY 10065, USA
[2]Department of Biochemistry, Albert Einstein College of Medicine, Bronx, NY 10461, USA
[3]Department of Bioengineering and Therapeutic Sciences, Department of Pharmaceutical Chemistry, Quantitative Biosciences Institute, University of California, San Francisco, San Francisco, CA 94143, USA
[4]Structural Biology Resource Center, The Rockefeller University, New York, NY 10065, USA
[5]Laboratory of Mass Spectrometry and Gaseous Ion Chemistry, The Rockefeller University, New York, NY 10065, USA
[6]Senior author
[7]Lead contact
*Correspondence: nketaren@rockefeller.edu (N.E.K.), rout@rockefeller.edu (M.P.R.)
https://doi.org/10.1016/j.str.2025.01.019

SUMMARY

Nanobodies are single domain antibody variants proving themselves to be compelling tools for research, disease diagnostics, and as therapeutics targeting a myriad of disease agents. However, despite this potential, their mechanisms of paratope presentation and structural stabilization have not been fully explored. Here, we show that unlike monoclonal antibodies, a nanobody repertoire maximizes sampling of an antigen surface by binding a single antigen in at least three different orientations, which are correlated with their paratope composition. Structure-guided reengineering of several nanobodies reveals that a single point mutation within the paratope or a highly conserved region of a nanobody's framework 3 (FR3) can markedly improve antigen affinity, nanobody stability, or both. Conversely, we show the negative impact on antigen affinity when "over-stabilizing" nanobodies. Collectively our results provide a universal strategy to tune a nanobody's affinity by modifying specific residues that can readily be applied to guide nanobody optimization and functionalization.

INTRODUCTION

In nature, there exist antibody variants composed solely of IgG heavy-chain glycoproteins, rather than the heavy-chain/light-chain pairs found in conventional IgG antibodies. These heavy-chain only antibodies (HCAbs), occurring in members of the family *Camelidae* and other lineages, can bind antigens with the selectivity and affinity equivalent to conventional antibodies.[1] The antigen binding domain of HCAbs is called the V_HH domain, and can be independently expressed as a fragment often termed a *nanobody*[1]. At a mere ~15 kDa, nanobodies are only one-tenth the size of conventional antibodies, which enables them to penetrate and access epitopes on antigens that are inaccessible to conventional antibodies.[2,3] Nanobodies generally have high intrinsic solubility and stability in varying environments, and their comparatively low structural complexity (including the absence of glycosylation sites) allows them to be produced in bacteria at quantity using standard techniques.[4–6] These properties make nanobodies a powerful complementary technology to conventional monoclonal antibody-based research reagents, diagnostics, and therapeutics,[6,7] recently gaining significant traction as promising therapeutics for the treatment of SARS-CoV-2.[8–11]

The structure of nanobodies is homologous to the variable fragment heavy chain (VH) domain of conventional antibodies, formed from a standard Ig fold with three complementarity determining regions (CDR1, CDR2, and CDR3) that typically create the paratope—the region on an antibody/nanobody that interacts with the antigen—separated by four framework (FR) regions that form the scaffold.[12–14] However, three notable differences distinguish nanobodies from VH domains: first, nanobodies possess on average a significantly longer CDR3 than is found in conventional antibodies,[1] second, the surface-exposed FR2 region of nanobodies is more hydrophilic, correlating with the loss of dimerization with the absent variable fragment light chain (VL) domain and third, many nanobodies have a second disulfide bridge linking their longer CDR3 to the FR.[15]

Engineering and functionalization of nanobodies is often required when moving from the bench to the clinic—in particular, optimization of biophysical properties (solubility, stability etc.) and minimization of antigenicity via humanization. Humanization

Please cite this article in press as: Ketaren et al., Unique mechanisms to increase structural stability and enhance antigen binding in nanobodies, Structure (2025), https://doi.org/10.1016/j.str.2025.01.019

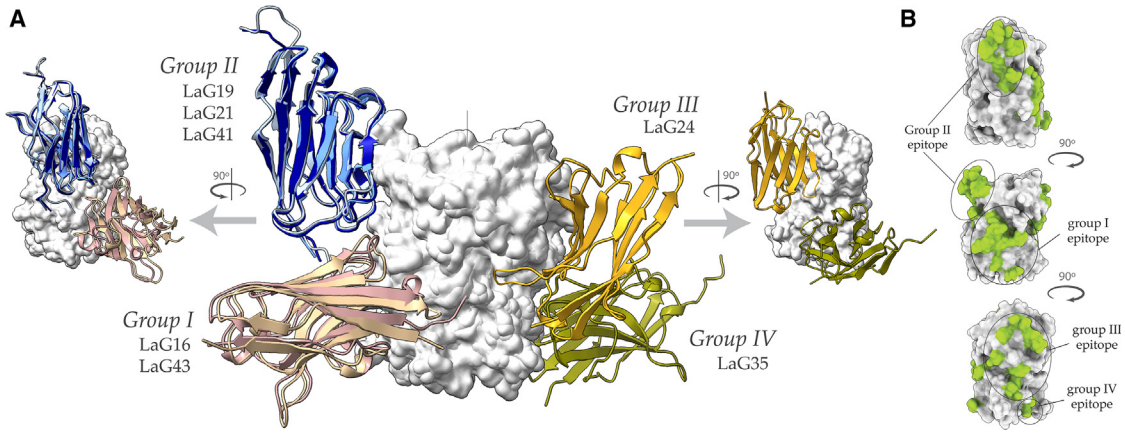

Figure 1. Crystal structures of 7 nanobody-GFP complexes

(A) The seven nanobody-GFP structures are aligned via their GFPs (in *gray*, represented as a surface rendered structure), where each nanobody is categorized into their respective group (groups I, II, III, and IV) based on their binding epitope on GFP.

(B) Mapping of the four epitope groups (in *green*) on the structure of GFP (*gray*) at three different viewpoints (90° rotations). Structure representations created using ChimeraX.[42]

efforts have generally focused on mutating the more hydrophilic FR2 region to better mimic the human VH domain, though such efforts can result in loss of antigen binding or nanobody aggregation.[16] Prior studies have also explored factors that contribute to the inherent stability, specificity and affinity of nanobodies,[17–21] including, for example, the roles of intramolecular disulfide bonds[15] and key FR residues,[21,22] though the generality of these findings remains unclear. By solving and analyzing seven nanobody-GFP complexes and systematically comparing our findings with other available structures, we showcase the unique ways nanobodies typically maximize their accessible surface area to bind their antigens. These structures also guided successful paratope and framework reengineering—the latter revealing the unique stabilizing role of FR3 to uncover generalizable mechanisms in nanobodies that contribute to their intrinsic stability. These findings, unique to nanobody-antigen interactions, can be readily implemented to rationally guide both nanobody humanization and the enhancement of nanobody stability and/or affinity, particularly in the development of nanobodies as therapeutics and diagnostics.

RESULTS

Nanobodies in a single repertoire bind their antigen in different orientations to maximally sample their cognate antigen surfaces

We solved the crystal structures of seven nanobodies in complex with green fluorescent protein (GFP; Figure 1A; Table 1) to reveal significant sampling of the GFP surface area by the nanobodies' epitopes (Figures 1A and 1B). The seven nanobodies were categorized into four distinct epitope regions designated groups I, II, III, and IV (Figure 1). Groups I, II, and III corroborate the lower resolution epitope mapping of Fridy et al.,[4] placing LaG16[23,24] and LaG43 in group I; LaG19, LaG21, and LaG41 in group II; and LaG24 in group III; in addition, a fourth epitope was mapped in this study (group IV) for LaG35 (Figure 1B). Superposition of the seven nanobody-GFP structures revealed that the nanobodies assume different orientations when bound to GFP, where nanobodies within a group conformed to a single orientation (Figure 1). Observations of nanobodies interacting in diverse orientations with their antigen have been reported in previous studies looking at numerous unrelated nanobody-antigen structures[3,25,26]; what is unique to this study is that we captured these observed diverse nanobody orientations from a repertoire of only seven nanobodies that were isolated from a single llama's immune response to a common antigen, GFP,[4] indicating that this is a common feature of HCAb epitope recognition. This repertoire of diverse orientations increases the potential for multiple nanobodies to bind a single antigen simultaneously, as shown in our study, where a mixture of nanobodies—one from each of the non-overlapping four epitope groups—can potentially bind simultaneously to GFP with no steric clashes (Figure 1A).

A nanobody's paratope composition dictates its orientation when bound to its antigen

Analysis of the interaction interface between each of the seven nanobodies and GFP (Figure 2A), revealed that each nanobody's orientation when bound to GFP was dictated by its paratope composition. For all group II nanobodies, LaG19, LaG21, and LaG41 (all closely related sequences), the CDR3 loop dominates the paratope composition by forming numerous interactions with GFP (Table S4). In doing so this orients the nanobodies to bind GFP in what can be described as an unorthodox "side-on" antigen-binding orientation that we refer to as "side-on CDR3" (Figure 2A). In comparison, group I nanobodies (LaG16 and LaG43) bind GFP via all three CDR loops, binding GFP in what can be described as a more orthodox "head-on" orientation (Figures 2A; Table S4) closely resembling that of conventional antibodies (Figure S1). LaG16 additionally recruits a "4th loop" from within its framework 3 region (FR3) to interact with GFP, where Arg78 forms an electrostatic interaction with Glu17 of GFP (Figure 2A). Remarkably, this additional loop is recruited to the paratope in numerous nanobodies,[27] where it sits next

Please cite this article in press as: Ketaren et al., Unique mechanisms to increase structural stability and enhance antigen binding in nanobodies, Structure (2025), https://doi.org/10.1016/j.str.2025.01.019

CellPress

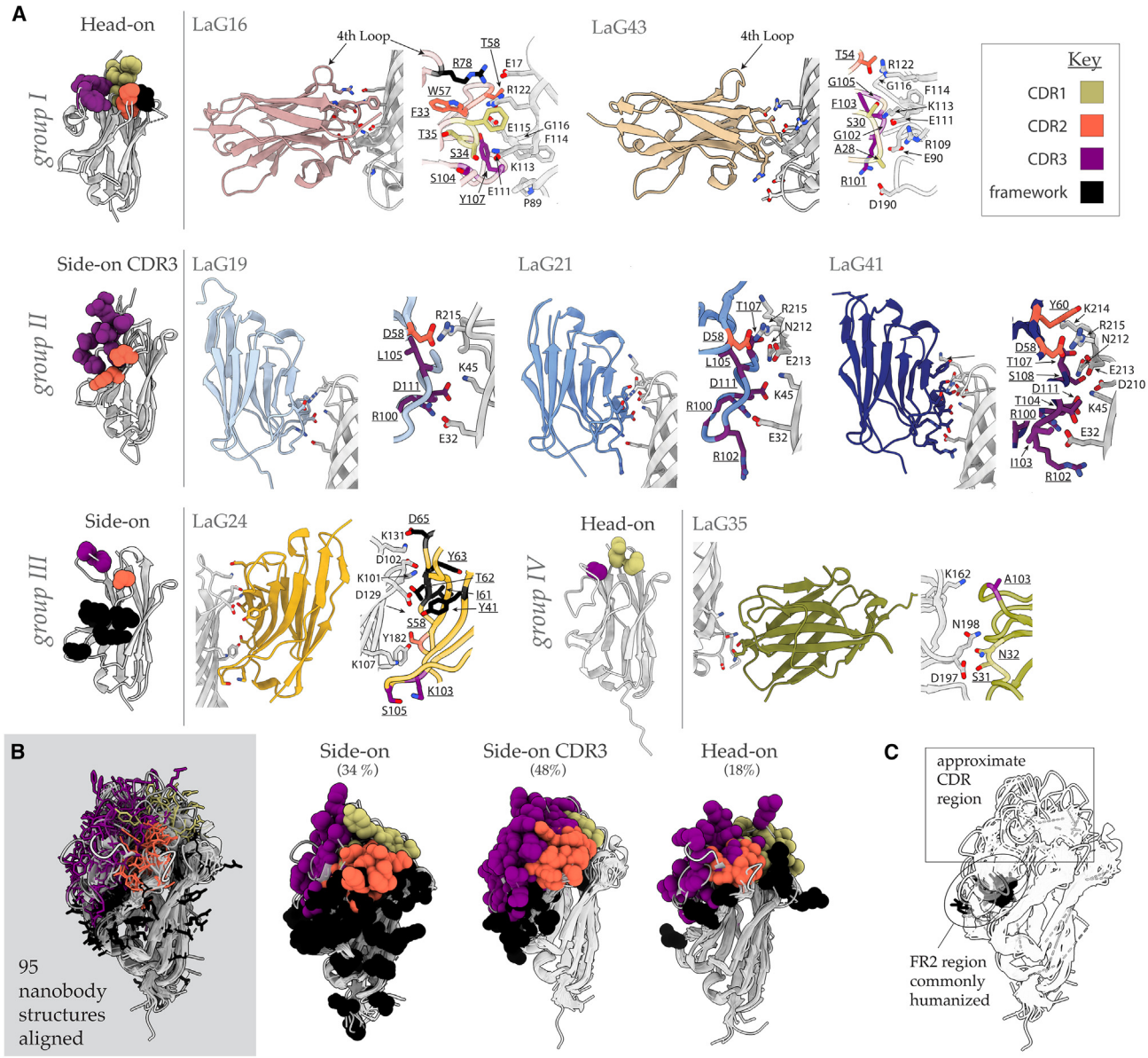

Figure 2. The composition of nanobody paratopes

(A) The seven nanobody-GFP structures are categorized into their respective epitope groups, and also shown is the "paratope category" they belong to: *side-on*, *side-on CDR3*, and *head-on,* determined by their orientation when bound to GFP. A close-up of each nanobody-GFP interaction is shown, with a detailed look at each interaction interface. The paratope residues of each nanobody are colored according to the color *key*, showing how paratope category is correlated to the contribution of different structural regions to antigen binding.

(B) Composite of the three paratope categories highlights the degree of chemical space utilized across the 95 nanobodies analyzed, with further categorization of the 95 structures into the three paratope categories (refer to Table S2 for PDBs). Each residue that participates in binding adopts the same color scheme as (A).

(C) The same alignment of the 95 nanobodies as (B), highlighting amino acids (black sticks) commonly humanized within FR2, from nanobodies that use these amino acids for antigen binding. Structure representations created using ChimeraX.[42]

to the canonical CDR loops, making it in essence function as a fourth small CDR. This fourth loop has reduced size and structural diversity compared to the other three CDRs, yet contributes an essential additional binding functionality. Similar to the group II nanobodies, LaG24 (group III) interacts in a "side-on" orientation with GFP, but rather than a CDR3-dominated interface, this is achieved through similar contributions to binding from both its CDR and FR residues, where over half its paratope is formed by FR residues (Figures 2A; Table S4). LaG24 has a much shorter CDR3 (9 residues in length) compared to the other six nanobodies (16–23 residues) (Figure S2), which exposes its FR regions to interact with GFP (Figure S3). This is also observed with other side-on interactors from previously published structures (Figure S4). LaG24's FR2 and FR3 both interact with GFP, where the latter is home to its only salt bridge with GFP (Asp65 interacts with Lys131 on GFP). This salt bridge is located at the periphery

Please cite this article in press as: Ketaren et al., Unique mechanisms to increase structural stability and enhance antigen binding in nanobodies, Structure (2025), https://doi.org/10.1016/j.str.2025.01.019

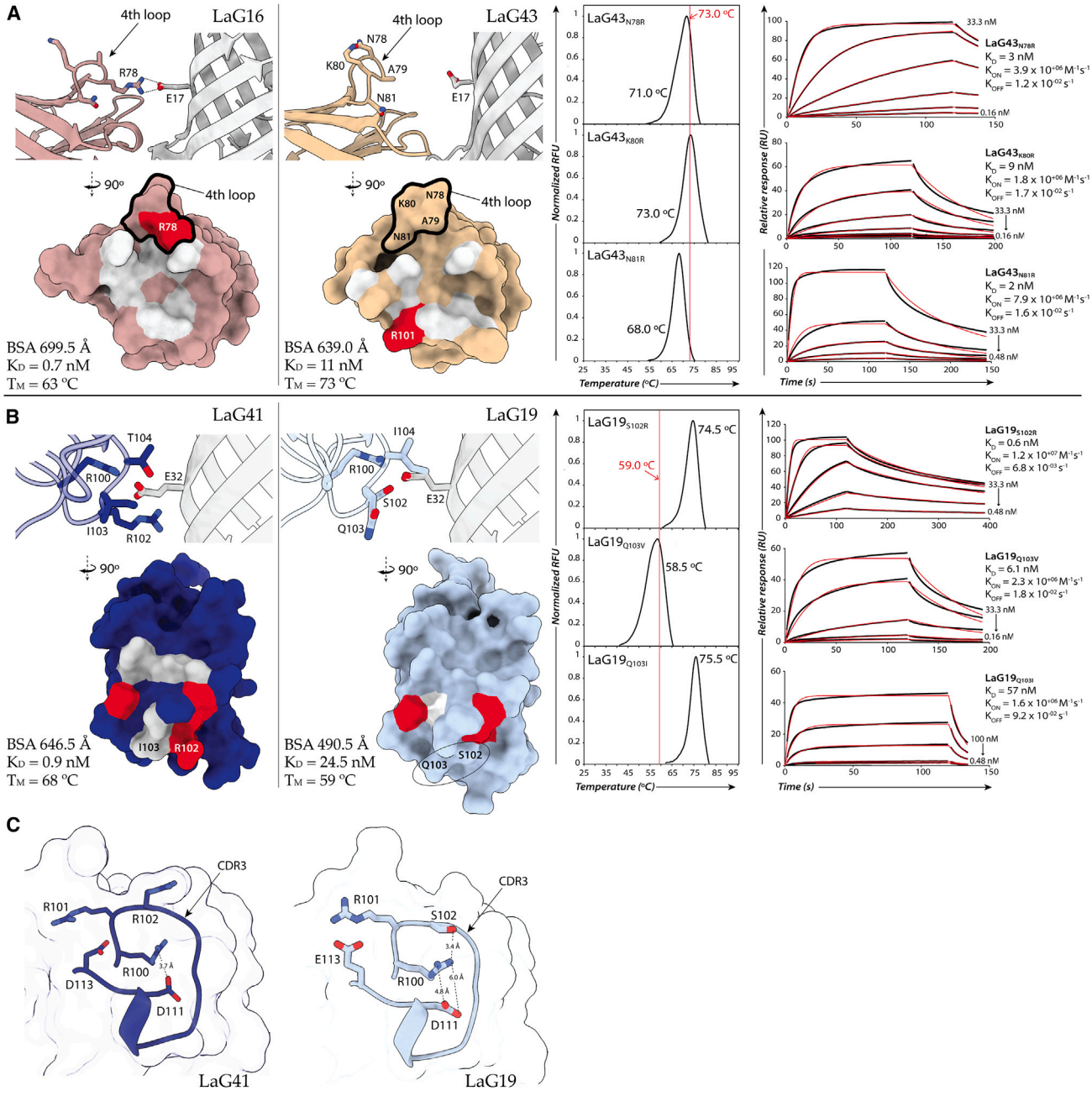

Figure 3. Structure guided paratope optimization

The interfaces of the nanobody-GFP complexes were analyzed using PDBePISA[40] revealing total buried surface area (BSA) for each nanobody and the key residues involved in interacting with GFP (colored *gray*). The surface rendered structure representations are color-coded as follows: salt bridges (*red*), hydrogen bonds (*white*).

(A) Comparison of the interaction interface of the high affinity GFP binder LaG16 (*pink*, far left) and the weaker GFP binder LaG43 (*tan*, middle left). Shown is a close-up of the 4th loop region of LaG16 and LaG43, highlighting the interaction between LaG16's Arg78 with Glu17 of GFP, the equivalent interaction is absent in LaG43. The surface rendered representation of both LaG16 and LaG43, outlines the key 4th loop region (in *black*), identifying location of Arg78 on LaG16 and residues on LaG43 that were mutated to promote an interaction between its 4th loop of and Glu17 on GFP. DSF results are plotted for each variant with the T_M of LaG43 indicated (*red* line) (middle right). SPR sensograms (far right) of each LaG43 variant are plotted displaying T_M values and binding kinetics/K_D values respectively with fits displayed in *red*.

(B) Comparison of the interaction interface of the strong GFP binder LaG41 (*dark blue*, far left) to the weaker GFP binder LaG19 (*light blue*, middle left). A close-up of the key LaG41 interacting residue, Arg102, and the equivalent that is absent in LaG19. A surface representation comparing the interaction interface of LaG41 and LaG19, reveals a greater hydrogen bond network in LaG41 compared to LaG19 and an extra salt bridge that is absent in LaG19, encircled in *black*. DSF

(legend continued on next page)

Please cite this article in press as: Ketaren et al., Unique mechanisms to increase structural stability and enhance antigen binding in nanobodies, Structure (2025), https://doi.org/10.1016/j.str.2025.01.019

of the paratope (Figure 2A), which may serve to secure the paratope in place. Additionally, Tyr41 within LaG24's FR2 forms an H-bond with Asp129 on GFP. Interestingly (and concerningly; see also in the following text), Tyr41 is one of the residues within FR2 often mutated to humanize nanobodies[16,28–30] (Figure 2C).

New generalizable categorization of paratopes

Collectively, the structures allowed us to classify our nanobodies into three universal paratope categories (Figure 2A): (1) side-on CDR3—where antigen binding is primarily via the CDR3; (2) head-on—where antigen binding is due to significant contributions from all three CDRs, which is similar to conventional antibodies; and (3) side-on interactors, where antigen binding results from significant contributions from both the FR and CDRs (Figure 2A). We investigated whether this classification system applied to other known nanobody-antigen interactions, and so performed a meta-analysis of 95 non-redundant nanobody-antigen complexes (Table S1) available to date from the Protein Data Bank (PDB, www.rcsb.org). We analyzed their paratope composition and orientation when bound to their antigen using PDBePISA,[31] visual inspection via PyMoL (Schrodinger LLC 2015) and with information from their respective publications. Our analyses revealed that the three categories of interactors we deduced from our seven crystal structures could be readily used to classify the 95 structures into the same three groups (side-on, side-on CDR3, and head-on) (Figure 2B). Our results revealed that "side-on CDR3" interactors predominate (48%) followed by "side-on" interactors (34% of the observed orientations), whereas "head-on" interactors are surprisingly the most infrequent (18%).

Re-engineering nanobody paratopes to create high-affinity binders from low affinity binders

Guided by the structures, we aimed to increase the GFP-binding affinities of two of our lower-affinity anti-GFP nanobodies (LaG43 and LaG19) for GFP by reengineering their paratopes. The group I nanobody, LaG43, has a ~10-fold lower affinity for GFP (K_D = 11 nM) compared with the other group I nanobody LaG16 (K_D = 0.7 nM). Both nanobodies bind head-on (see previously) and have overlapping epitopes, yet LaG16 utilizes Arg78 on its "4th loop" within FR3 to form its only salt bridge with GFP (Glu17) (Figure 3A). This interaction may serve to "lock" LaG16 into its head-on orientation, drawing its surface toward GFP, as reflected by the increased number of H-bonds at the interface (Table S4) and its higher affinity for GFP compared to LaG43. We thus aimed to recruit the equivalent 4th loop in LaG43 into a similar electrostatic interaction with GFP as seen with LaG16. We constructed the following three LaG43 variants by introducing an arginine at three different positions along the 4th loop: LaG43$_{N78R}$, LaG43$_{K80R}$, and LaG43$_{N81R}$. The binding affinities determined by surface plasmon resonance (SPR), revealed all LaG43 variants increased in affinity for GFP compared to wild-type (Figure 3A, *far right*). However, the GFP affinity of all LaG43 variants remained lower than that of LaG16, which may be due to the destabilization of a salt bridge formed between Arg101 on LaG43 and Asp190 on GFP (Figure 3A, *middle left*) by the newly introduced interaction point on the variants. SPR was also performed between the three LaG43 variants and a GFP variant with an alanine substituting Glu17 (GFP$_{E17A}$) to determine if the introduced Arg within each variant forms the same interaction with GFP (Glu17) as LaG16. LaG43$_{N78R}$ (the direct homologous mutation to LaG16's Arg78) displayed weaker binding for GFP$_{E17A}$, supporting the conclusion that the increased affinity for this variant resulted from an interaction between the introduced Arg and Glu17 on GFP (Figure S5). However, this binding pattern was not observed for LaG43$_{K80R}$ and LaG43$_{N81R}$—both showing stronger binding to GFP$_{E17A}$ compared with wildtype GFP suggesting a different set of interactions is formed between these two variants and GFP$_{E17A}$ not dominated by Glu17 on GFP. Interestingly, thermal denaturation measurements performed by differential scanning fluorimetry (DSF), showed a decreased T_M of the variants LaG43$_{N78R}$ and LaG43$_{N81R}$ (Figure 3A, *middle right*). The decreased T_M coupled with the SPR results for these two variants, suggests that Arg at these two positions slightly destabilizes the structures of these LaG43 variants, resulting in the formation of a more favorable set of interactions with GFP compared with wild-type LaG43 and LaG43$_{K80R}$, which both show higher intrinsic stability.

As mentioned earlier, CDR3 is the main point of interaction with GFP for the group II nanobodies, which all share high sequence homology with almost identical CDR3 loops (Figure S2). As such, all group II nanobodies have very similar structures when bound to GFP. However, LaG19 has a 27-fold weaker affinity for GFP (K_D = 24.9 nM) compared to the highest affinity group II nanobody LaG41 (K_D = 0.9 nM). We created a series of LaG19 point mutants to explore different ways to increase the affinity of LaG19 for GFP. One hypothesis for the LaG19's reduced affinity for GFP is due to LaG19 having a serine at position 102 (Figure 3B, *middle left*) instead of an arginine as seen in the other group II nanobodies (Figure S2). In LaG41 and LaG21, Arg102 forms several key interactions with GFP, including an electrostatic interaction with Glu32 (Table S4) (Ser102 in LaG19 does not participate in binding to GFP). To probe the essentiality in GFP binding affinity due to the Arg at position 102, we created the point mutant, LaG19$_{S102R}$, which incorporates the key serine to arginine substitution (Figure 3B). SPR revealed LaG19$_{S102R}$ displayed a >40-fold increase in affinity for GFP (K_D = 0.6 nM) (Figure 3B, *top*, *far right*) compared to wild-type LaG19, making its affinity comparable to LaG41 (K_D = 0.9 nM). To support the hypothesis that the interaction is between Arg102 in the variant and Glu32 on GFP, SPR was performed with LaG19$_{S102R}$ against a point mutant of GFP in which Glu32 is substituted with an alanine (GFP$_{E32A}$). The SPR results revealed undetectable binding of LaG19$_{S102R}$ (Figure S5) for

results are plotted for each variant with the T_M of LaG19 indicated (*red* line) (middle right). SPR sensograms (far right) of each LaG19 variant are plotted displaying T_M values and binding kinetics/K_D values respectively with fits displayed in *red*.

(C) A detailed view of the CDR3 region surrounding amino acid 102 for LaG41 and LaG19. For LaG41, the triple arginine motif formed from Arg100, Arg101, and Arg102 repels Arg100 and Arg101 from Arg102 to promote their interaction with adjacent basic residues. For LaG19, Ser102 interacts with Arg100, with large distances between Arg100 and Asp111. The longer side chain of Glu111 in LaG19, promotes an interaction with Arg101. The atomic distances between the interacting amino acids are represented as dashed lines with the distance in Å stated for each interaction. Structure representations created using ChimeraX.[42]

Please cite this article in press as: Ketaren et al., Unique mechanisms to increase structural stability and enhance antigen binding in nanobodies, Structure (2025), https://doi.org/10.1016/j.str.2025.01.019

GFP_{E32A}, suggesting the electrostatic interaction formed between Arg102 and Glu32 is essential for the interaction with GFP. Interestingly $LaG19_{S102R}$ showed an increase in its intrinsic stability by 15°C compared with wild-type LaG19(Figure 3B, *top*, *middle right*). In LaG41, Arg102 is a member of a triple arginine motif with Arg100 and Arg101 (Figure 3C). The concentration of like charges at this region presumably repels Arg100 and Arg101 from Arg102, bringing them closer to two adjacent acidic residues (Asp111 and Asp113) also located on CDR3 (Figure 3C, *left*). The repelled arginines are in better proximity to interact with their nearby acidic residues, which may serve to stabilize the CDR3 loop. By stabilizing the CDR3 loop, this could serve to stabilize the overall nanobody structure, which may explain the 15°C increase in T_M of $LaG19_{S102R}$. Additionally, the equivalent of Asp113 in LaG19 is Glu113 (Figure 3C, *right*)—thus the longer side chain of glutamate may further promote a stable interaction with the repelled Arg101 in $LaG19_{S102R}$, adding to the higher stability of the variant over both wild-type LaG19 and LaG41.

We created an additional two point mutants of LaG19: $LaG19_{Q103V}$ and $LaG19_{Q103I}$, to test whether hydrophobic amino acids within the paratope region promoted antigen affinity, as hydrophobic amino acids are highly represented in the paratopes of nanobodies.[27] $LaG19_{Q103I}$ exhibited a large increase in T_M (~16°C) over wild type that is similar to $LaG19_{S102R}$; however, unlike $LaG19_{S102R}$, it had a ~2-fold decrease in affinity for GFP (K_D = 57 nM) compared to wild type (Figure 3B). It is possible that the introduction of a hydrophobic isoleucine in this solvent-exposed region of CDR3 (Figure S6) creates a local region of stability on CDR3 that draws CDR3 away from the surface. This in turn stabilizes the nanobody structure (as reflected by the large increase in T_M) yet restrains the ability of CDR3 to interact with GFP resulting in the observed decrease in affinity of the variant. Conversely, $LaG19_{Q103V}$ had an increase in affinity for GFP over wildtype (K_D = 6.1 nM), yet no significant change in T_M.

A conserved region of framework 3 plays a key role in nanobody stability

The FR3 of our repertoire of anti-GFP nanobodies revealed a number of single amino acid differences within individual nanobodies that deviated from the consensus sequence produced by all seven nanobodies (Figure S2). One difference (as seen previously) resulted in the recruitment of the 4th loop of LaG16 to interact with GFP (Figure 3A). Structural mapping of the four remaining single amino acid differences (Figure S7) that deviated from the repertoire's consensus sequence, localized all four amino acid substitutions within the proximity of two loops region found within FR3, which are both parallel to one another and adjacent to the three CDR loops that are largely responsible (though in differing capacities) for binding GFP. One substitution found in LaG21 saw a leucine replace a highly conserved phenylalanine residue at position 69 (Figure 4A, *top*; Figure 5A). In six of the seven nanobody structures, this highly conserved phenylalanine at position 69 forms an interaction with the sulfur group of an adjacent highly conserved methionine residue (Figure 4A, *top*). Interactions between methionine and aromatic amino acids are documented to be an important, evolutionarily conserved stabilizing interaction within protein structures.[17–19] With a Leu at position 69, LaG21 lacks this stabilizing interaction. We created a LaG21 variant by substituting Leu69 with phenylalanine ($LaG21_{L69F}$) to investigate whether the conservation of this phenylalanine is due to its role in stabilizing a nanobody's structure. DSF results showed a large, ~9°C, increase in the T_M of $LaG21_{L69F}$ (T_M = 64°C) compared to wildtype LaG21 (T_M = 55°C) (Figure 4A, *middle*) and SPR of $LaG21_{L69F}$ revealed a 10-fold increase in affinity (K_D = 0.7 nM) for GFP over wild-type LaG21 (K_D = 7 nM), bringing its affinity on par with the strongest binder to GFP of the group II nanobodies (LaG41). This result reveals the role of this conserved Phe69 in both nanobody stability and antigen affinity.

The three additional sites within FR3 on our anti-GFP nanobodies that deviate from the consensus FR sequence were also observed to have a stabilizing role (Figures 4B–4D). The first site was Glu91 on LaG16 (this residue has also shown to be stabilizing in a previous study[21]), located on a loop within FR3 that the four stabilizing sites are centered, is flanked on either side by two conserved acidic amino acids (Asp94 and Glu93) (Figure 4B, *top*). The clustering of like charges increases the likelihood of coulombic repulsion, known to decrease protein stability.[20] In the other six nanobodies, a lysine is present in place of this glutamate, which in contrast to Glu91, would neutralize the effect of charge repulsion, creating local stabilization within the loop. To test this possible stabilizing effect induced by lysine at this position, we constructed a $LaG16_{E91K}$ variant and assessed its stability and binding (Figure 4B). Our DSF data showed the T_M of the variant did indeed increase by 3°C compared to wild type, without impairing affinity (Figure 4B; Table S3). The second site identified was Gln68 of LaG24, located on the same loop as Glu91 from LaG16 (Figure 4C). This residue is a lysine in the other six nanobodies, and this lysine interacts with a nearby conserved aspartate residue (Figure 4C). We hypothesize that the interaction between lysine and aspartate serves to stabilize this loop region. We constructed and tested a LaG24 point mutant substituting glutamine with lysine, $LaG24_{Q68K}$. Our DSF results revealed a 2°C increase in thermal stability coupled to an almost 10-fold increase in affinity of $LaG24_{Q68K}$ over wild type (Figure 4C; Table S3). The third site identified was His85 on LaG24, which in the other six nanobodies is a glutamine that forms a key interaction with a conserved Arg23 located within FR1 (Figure 4D). The location of His85 on LaG24 is near a loop within the same region of FR3 as the other three sites. In LaG24, the side chains of His85 and Arg23 are flipped away from each other (Figure 4D), where His85 interacts instead with Ser74. We created a LaG24 variant ($LaG24_{H85Q}$), substituting His85 with glutamine to create an interaction partner for Arg23 analogous to the other six nanobodies. Similar to the other three sites, $LaG24_{H85Q}$ had an increase in thermal stability (by 2°C) coupled to a >10-fold increase in affinity for GFP (Figure 4D; Table S3).

Molecular modeling provides further mechanistic insight into the effect of framework 3 stabilization on nanobody function

To explore the possible mechanism behind both the stabilizing effect and increased antigen affinity induced by the FR3 point mutants, we assessed the effect on the structure of LaG21 resulting from the Leu69Phe substitution by performing molecular

Please cite this article in press as: Ketaren et al., Unique mechanisms to increase structural stability and enhance antigen binding in nanobodies, Structure (2025), https://doi.org/10.1016/j.str.2025.01.019

CellPress

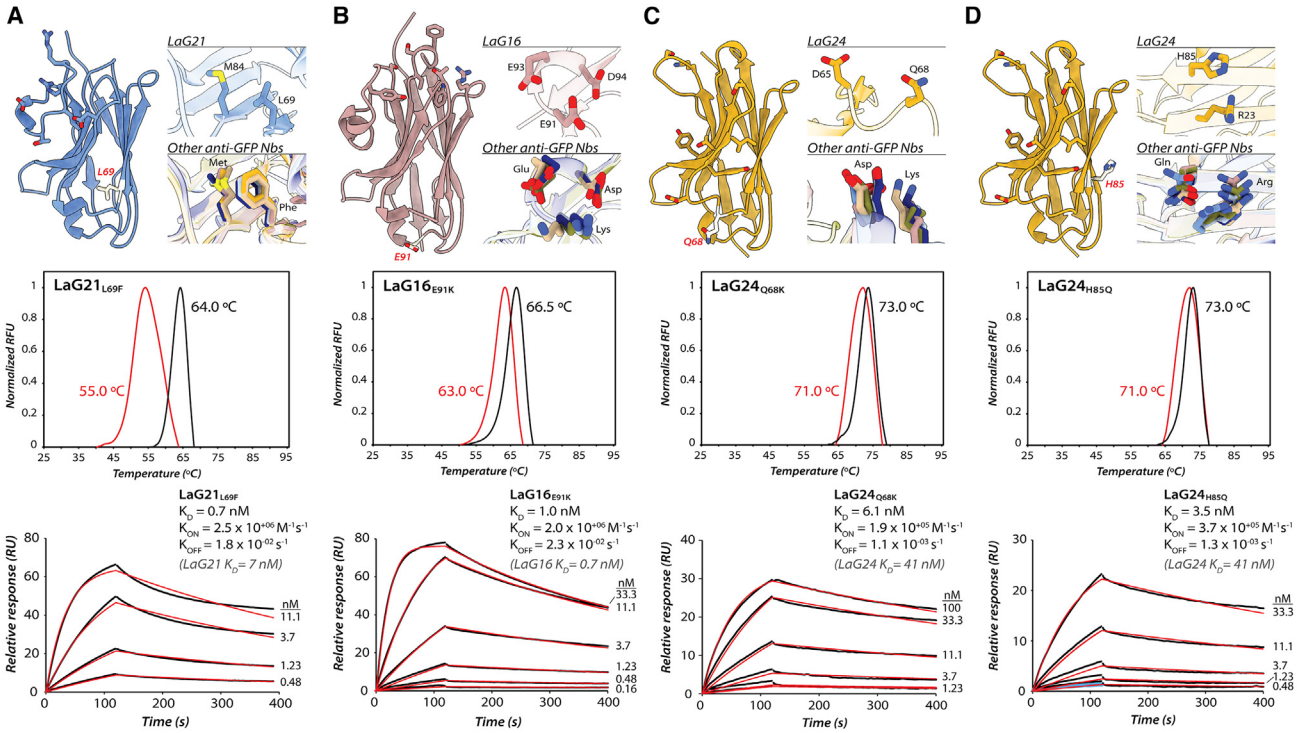

Figure 4. Framework optimization of anti-GFP nanobodies

(A–D) shows the rationale behind each FR optimizing mutation and the results of their characterization using DSF (wild-type and variant TM is noted in *red* and *black*, respectively) and SPR (fits are displayed in *red*) revealing T_M and kinetic/K_D values compared to wildtype. The position of each mutated FR residue is colored *white* and represented in *stick form* on the structure of the respective nanobody. The paratope of each nanobody is also shown, represented as sticks. (A) $LaG21_{L69F}$ rationale, with close-ups of LaG21's highly conserved methionine (Met84) pointed away from Leu69 and the equivalent residues in the other six anti-GFP nanobodies where Phe is in close proximity to the sulfur group of the highly conserved methionine. (B) $LaG16_{E91K}$ rationale, showing a detailed view of Glu91 of LaG16 flanked by two conserved acidic residues (Glu91 and Glu93) in comparison to Lys91 in the other six anti-GFP nanobodies flanked by the same highly conserved acidic residues. (C) $LaG24_{Q68K}$ rationale, with close-ups of Gln68 of LaG24 flipped away from the acidic Asp65 unlike in the other six nanobodies, where the basic lysine residue is oriented toward the acidic aspartate residue. (D) $LaG24_{H85Q}$ rationale, with close-ups of Arg23 on LaG24 flipped away from His85, in comparison to the interaction of Gln85 with arginine present in the other six anti-GFP nanobodies. Structure representations created using ChimeraX.[42]

dynamics (MD) simulations of wild-type LaG21 and the FR optimized LaG21 ($LaG21_{L69F}$). The MD simulations were performed at three temperatures beginning at room temperature (300 K) then 336 K and 421 K, where the last serves as a control reflecting expected thermal destabilization and unfolding for both the wild-type and FR optimized LaG21. Our original hypothesis (see previously) is that the Leu69Phe substitution results in an interaction of the phenylalanine with an adjacent methionine that stabilizes FR3, which in turn stabilizes the overall structure of the nanobody resulting in better binding to GFP (Figure 4A). The MD simulations revealed that LaG21 has an overall greater degree of motion in its structure compared to $LaG21_{L69F}$ (Figure 6A). This degree of fluctuation is greater for residues within the CDRs, especially CDR3, which is the main interaction point of LaG21 with GFP (Figure 2A). In comparison, $LaG21_{L69F}$ consistently maintains low RMS fluctuations across its whole structure (Figure 6). To probe the cause of the differences in the structural dynamics between LaG21 and $LaG21_{L69F}$, we performed mutual information (MI) analysis[32] on the MD simulations, which allows us to observe correlated dynamics between backbone dihedral angles of residue pairs in the wildtype and mutant LaG21 structures. A higher MI between residues indicates that their backbone conformations are correlated, while a lower value indicates that their motions are nearly independent of each other. Our results reveal that the wild-type LaG21 shows a high degree of correlation between residue pairs in general, with significant correlations between CDR3 and FR2 as well as between CDR3 and the beginning of FR3, which is the location of the Leu69Phe substitution (Figure S10). Therefore, it is likely that the FR3 dynamics of LaG21 directly drive structural changes in its paratope, while the Leu69Phe mutation suppresses such an influence. These results support our hypothesis that stabilizing FR3 is indeed stabilizing the overall structure of LaG21, due to FR3's direct influence on CDR3, where the decreased fluctuations of $LaG21_{L69F}$'s CDR3 likely promotes higher intrinsic stability and favorable binding to GFP, resulting in the observed high affinity interaction with GFP. This hypothesis is consistent with the importance of the stabilization of CDR3 for the interaction of other group II, side-on CDR3 binders (see aforementioned example with LaG41 and LaG19).

Applying general framework 3 optimization principles to nanobodies with therapeutic potential

We tested the generalizability of implementing three of the four conserved framework stabilization principals identified

Please cite this article in press as: Ketaren et al., Unique mechanisms to increase structural stability and enhance antigen binding in nanobodies, Structure (2025), https://doi.org/10.1016/j.str.2025.01.019

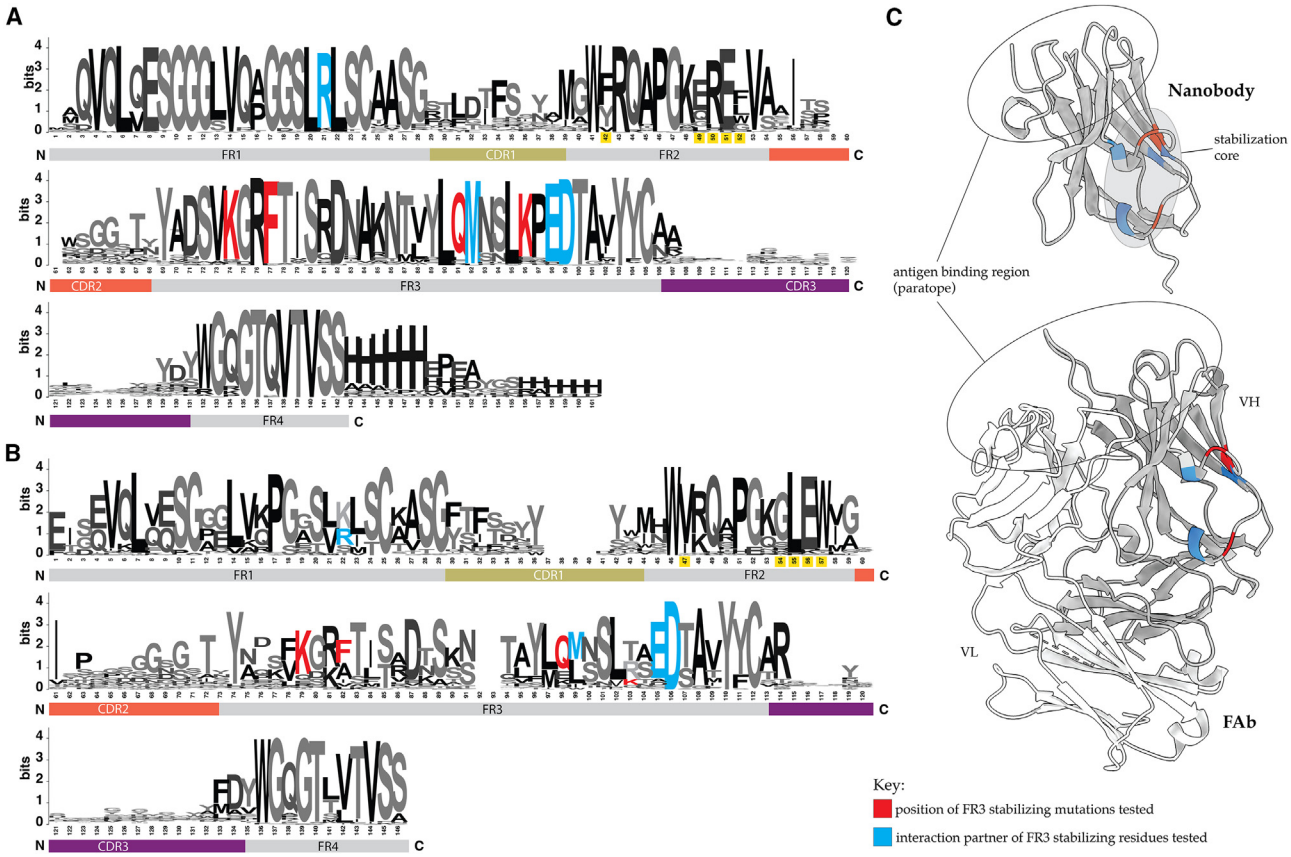

Figure 5. Comparing the level of sequence conservation between nanobodies and human VH domains

(A and B) Sequence alignment of 95 nanobody sequences (refer to Table S1 for PDBs) (A) and 87 VH domain sequences (refer to Table S2 for PDBs) (B). The FR residues mutated and identified as stabilizing for nanobodies are colored according to the displayed key. The FR2 residues that differ between nanobodies/VHH and VH and are commonly humanized have their sequence number shaded in yellow on each alignment.

(C) The structure of a representative nanobody (top, LaG41 structure) and FAb (PDB ID: 1bj1), highlighting the location of the nanobody FR3 stabilizing amino acids, which are colored according to the displayed key. Structure representations created using ChimeraX.[42]

previously, on a repertoire of anti-SARS-CoV-2 spike S1 nanobodies. These nanobodies were generated from our previous work[2] and were not isolated from the llama that produced the anti-GFP nanobodies used in this study. We had no atomic-scale structural information for these nanobodies, allowing us to test the ability of these stabilizing principles to be applied using only primary sequence-level information.

In total, we constructed eight variants of eight different SARS-CoV-2 anti-spike S1 nanobodies (Table S8), and the results of their characterization are summarized in Table 2. Importantly, the general trend is that these mutations result in both increased *stability* and *affinity*. For example, the nanobody S1-40, with an affinity to spike protein too low to obtain a reliable SPR result (likely sub-micromolar K_D), was a candidate for the introduction of a lysine at residue 89 to reduce coulombic repulsion (based on LaG16$_{E91K}$ seen previously). The resulting variant S1-40$_{S89K}$ displayed a ~2°C increase in T_M over wild type, coupled to a remarkable 0.5 nM K_D affinity for spike. This substitution not only "rescued" the binding ability of the nanobody but also created a high affinity binder from a nanobody with undetectable binding. Similarly, creating the same stabilization site on nanobody S1-RBD-42 (to create the point mutant S1-RBD-42$_{E88K}$) resulted in both increased stabilization and affinity for spike over wild type (Table 2). One exception to the trend of increased affinity with increased structure stability is when the Phe-Met stabilizing interaction was introduced into an already high-affinity binder, S1-36 (K_D = 0.2 nM). The S1-36$_{L70F}$ variant, similar to LaG21$_{L69F}$, resulted in a large (~10°C) increase in T_M over wild type; however, unlike LaG21$_{L69F}$, S1-36$_{L70F}$ loses its ability to bind spike S1. This result is another example of the detrimental effect of over stabilizing a nanobody, which may serve to restrain a nanobody from interacting optimally with its antigen, a result here that is accentuated in an already highly stable, high-affinity nanobody. The only nanobody variant to exhibit a decrease in T_M was S1-RBD-14$_{E89K}$, which had a ~3°C decrease in T_M compared with wild type. The substitution introduced a lysine in FR3 in place of a glutamate (E89K), which was predicted to stabilize this loop region within FR3 by reducing coulombic repulsion. However, with this decrease in T_M came a dramatic ~80-fold increase in affinity of the S1-RBD-14$_{E89K}$ (K_D = 0.3 nM) over wild type (K_D = 25 nM), revealing another example of how relieving the intrinsic stability within the structure promotes higher affinity antigen binding.

Please cite this article in press as: Ketaren et al., Unique mechanisms to increase structural stability and enhance antigen binding in nanobodies, Structure (2025), https://doi.org/10.1016/j.str.2025.01.019

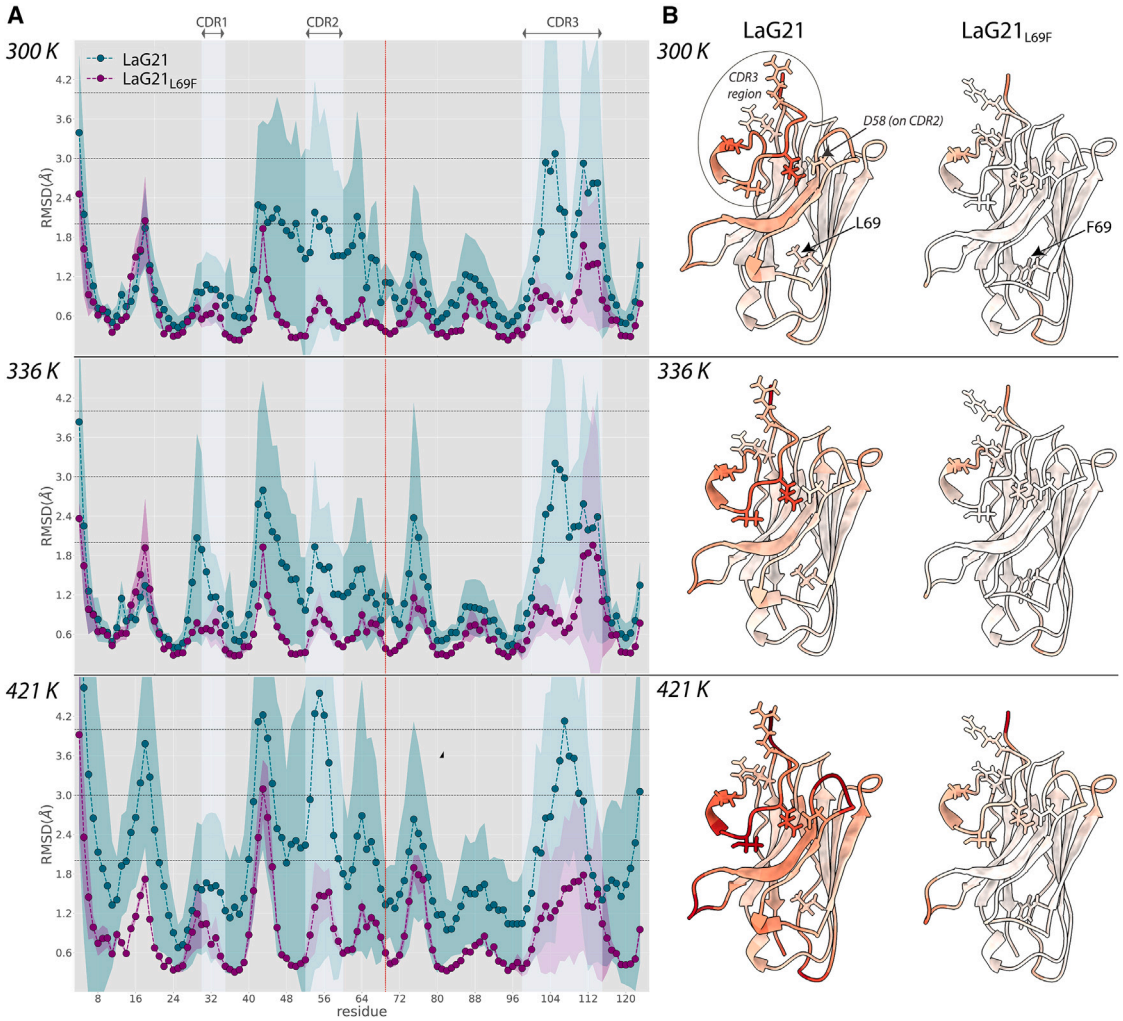

Figure 6. Molecular modeling of the conformational heterogeneity of LaG21

(A and B) present structural metrics computed from 1.6 μs molecular dynamics simulations of solvated LaG21 (in *teal*) and LaG21$_{L69F}$ (in *purple*) at three different temperatures 300, 336, and 421 K where the shaded regions show 95% confidence intervals. (A) The red vertical line denotes the location of the Leu69Phe mutation. In addition to CDR regions being labeled, FR and CDR regions are shaded vertically in *gray* and *light blue*, respectively. Average RMS fluctuations (y axis) per residue (x axis), relative to the energy minimized crystal structure at room temperature: both LaG21 and LaG21$_{L69F}$ consistently maintain 1.8–2 Å variation in CDRs 1 and 2 at low to moderate temperatures. LaG21 has a higher baseline RMSD in CDR3 and completely unfolds at higher simulation temperatures unlike LaG21$_{L69F}$. (B) Paratope residues are represented as sticks in addition to Leu69 (for LaG21 structures) and Phe69 (LaG21$_{L69F}$ structures). Per-residue RMS fluctuations at different temperatures normalized as a *Z* score between 0 (white) −100 (dark red) and projected on reference LaG21 and LaG21$_{L69F}$ structures. At near room temperature (300 K), LaG21 paratope residues Arg102, Leu105, Thr107, Asp111 show the most significant fluctuation from the crystal structure, while the Leu69Phe mutation makes the entire LaG21$_{L69F}$ CDR3 more stable, in addition to FR regions. Structure representations created using ChimeraX.[42]

DISCUSSION

Our results shed light on how nanobodies exploit their small structure and biochemical makeup to function as highly effective, single-domain antigen binders through the utilization of both their increased surface hydrophilicity and intrinsic stability. The meta-analysis revealed how antigen sampling is maximized through structural diversity of the camelid HCAb response, as observed even through our crystal structures alone. With FR residues playing a prominent role in binding, nanobodies targeting a single antigen bind in different orientations, which allows them to explore a greater relative surface area for their paratopes than conventional antibodies. The varied orientations different nanobodies adopt upon antigen binding may further enable the simultaneous binding of multiple nanobodies generated against the same antigen without steric hindrance.[2] This highlights the potential for synergy between different HCAbs during an immune response and consequently reveals how nanobodies are particularly tuned to work synergistically with other nanobodies. This phenomenon of synergy between nanobodies was observed in our work developing therapeutic nanobodies for the treatment of the SARS-CoV-2 virus, where a pair of nanobodies powerfully enhanced each other's interactions, to the point of their mixture being thousands of times more potent in viral neutralization than

Please cite this article in press as: Ketaren et al., Unique mechanisms to increase structural stability and enhance antigen binding in nanobodies, Structure (2025), https://doi.org/10.1016/j.str.2025.01.019

Table 1. Data collection and refinement statistics

Structure:		LaG16	LaG43	LaG24	LaG19	LaG21	LaG41	LaG35
PDB ID:		8SFS	8SLC	8G0I	8SFV	8SFX	8SG3	8SFZ
Data Collection								
	Space group	$P3_121$	P63	$P\ 2_12_12$	$I4_122$	I4	$I4_1$	$P22_12_1$
	Cell dimensions	*a* = 131.77 Å, *b* = 131.77 Å, *c* = 153.58 Å	149.43, 149.43, 127.01	82.1, 86.7, 52.1	111.25, 111.25, 193.8	111.12, 111.12, 194.20	108.63, 108.63, 198.74	69.65, 101.73, 184.48
		$\alpha = 90°, \beta = 90°, \gamma = 120°$	90, 90, 120	90, 90, 90	90, 90, 90	90, 90, 90	90, 90, 90	90, 90, 90
	Resolution (Å)	50.0–2.20 (2.24–2.20)	50.0–2.70 (2.75-2.70)	50.0–2.20 (2.26–2.20)	41.25–1.80 (1.83–1.80)	41.3–1.95 (2.00–1.95)	50–3.0 (3.05–3.0)	50.0–1.9 (1.93–1.9)
	R_{sym} or R_{merge}	0.107(0.962)	0.117(0.941)	0.089(0.726)	0.083(0.908)	0.130(1.403)	0.212(0.833)	0.086(0.314)
	$I/\sigma I$	22.6(1.67)	20.4(1.13)	22.4(2.61)	29.5(2.83)	11.1(2.0)	10.3(1.78)	14.8(1.51)
	Completeness (%)	95.9(69.0)	99.9(98.8)	99.5(93.4)	99.6(93.1)	94.4(81.88)	84.6(94.0)	91.2(62.8)
	Redundancy	10.4(8.4)	4.4(4.2)	10.0(6.2)	14.3(14.5)	15.1(12.7)	3.7(3.9)	3.8(3.1)
Refinement								
	Resolution (Å)	46.7-2.37	48.39–2.97	44.65–2.20	41.25–1.83	36.67–1.95	47.19–3.11	46.10–1.90
	No. reflections	62729	33003	18349	51900	80508	17265	103243
	R_{work}/R_{free}	0.1904/0.2170	0.2184/0.2399	0.1811/0.2413	0.1827/0.2059	0.2101/0.2275	0.2746/0.3044	0.2067/0.2312
	No. atoms							
	Protein	5563	5562	2632	2793	5402	2754	8284
	Ligand/ion	275	118	38	108	212	31	96
	Water	193	9	66	170	146	6	406
	***B*-factors**							
	Protein	56.96	69.71	44.78	45.13	50.84	77.80	46.59
	Ligand/ion	76.89	68.07	44.83	72.76	70.23	63.69	42.79
	Water	54.25	51.65	43.40	46.95	46.00	51.5	42.93
	r.m.s. deviations							
	Bond lengths (Å)	0.008	0.006	0.013	0.011	0.012	0.004	0.012
	Bond angles (°)	0.95	0.94	1.23	1.13	1.11	0.79	1.05

Values in parentheses are for highest-resolution shell.

Please cite this article in press as: Ketaren et al., Unique mechanisms to increase structural stability and enhance antigen binding in nanobodies, Structure (2025), https://doi.org/10.1016/j.str.2025.01.019

Table 2. Framework optimization of nanobodies generated against wild-type SARS-CoV-2 spike protein

Original mutation			T_M (°C)	K_D (M)
LaG21$_{L69F}$	Wild type	S1-8	74.0	3.8
	Mutant	S1-8$_{L70F}$	83.0	3.2
	Wild type	S1-28	66.0	0.6
	Mutant	S1-28$_{L70F}$	77.5	0.09
	Wild type	S1-36	66.5	0.2
	Mutant	S1-36$_{L70F}$	76.0	undetectable
LaG16$_{E91K}$	Wild type	S1-40	57.0	undetectable
	Mutant	S1-40$_{S89K}$	59.5	0.5
	Wild type	S1-RBD-14	65.0	25
	Mutant	S1-RBD-14$_{E89K}$	62.5	0.3
	Wild type	S1-RBD-42	42.0, 59.0	7.5
	Mutant	S1-RBD-42$_{E88K}$	64.0	0.1
LaG24$_{Q68K}$	Wild type	S1-14	59.5	2.4
	Mutant	S1-14$_{Q66K}$	61.0	1.7
	Wild type	S1-RBD-31	68.5	0.2
	Mutant	S1-RBD-31$_{Q67K}$	71.5	0.4

T_M and K_D values for wild-type S1-14, S1-28, S1-36 and S1-RBD-14 taken from Mast et al.[2]

Mutant nanobodies are the wild-type nanobodies incorporating the equivalent original mutation in column 1 (SPR and DSF data detailed in Figures S8 and S9).

each separately.[2] Additionally, we have demonstrated significant participation of nanobody FR residues in antigen binding (Figures 2A and 2B). Of particular note for the engineering of nanobody therapeutics, several of the 95 nanobodies we analyzed utilize sites in FR2 region for antigen binding that are often mutated for humanization purposes (Figure 2C). This observation highlights a potential problem with humanization efforts that target nanobody FRs, particularly FR2, as the FR can be integral for nanobody-antigen binding.

Our paratope reengineering work underscores how the structural stability of nanobodies influences antigen affinity, where the dynamics of the loops throughout the nanobody structure play an important role in mediating this effect. Firstly, for the paratope-optimized LaG19 nanobody, the correlation between the large increase in stability of LaG19$_{S102R}$ variants with a large increase in affinity for GFP leads us to hypothesize that the >40-fold increase in affinity is due to the cumulative effect of Arg102's stabilizing interaction formed with Glu32 on GFP, and the intra-loop stabilization executed by the triple arginine motif of CDR3—possibly an instance where a stabilized CDR3 promotes antigen binding. This reveals increased antigen affinity is the product of two components: (1) stabilization of the epitope-paratope interface, and (2) intra-stabilization of the paratope itself. It is known that the CDR3 loops of nanobodies are important for nanobody stability and solubility in cases where additional disulfide bonds and/or other non-covalent interactions directly stabilize these loops,[17,33] but unique here is a mechanism of intra-loop stabilization executed by the triple arginine motif and its impact on antigen affinity. Secondly, with the LaG19$_{Q103I}$ variant, "over-stabilization" of the structure possibly restrained the nanobody paratope from binding optimally to its antigen, as shown from the reduced affinity of the more stable variant. Lastly, corresponding to the previous finding, slightly *destabilizing* the nanobody paratope structure (LaG43 variants) correlated with *increased* antigen affinity, which suggests nanobodies need a degree of flexibility within their paratope to optimally bind its antigen.

Furthermore, our FR reengineering enabled us to pinpoint a region on nanobodies within FR3, distal to the CDR loops, that acts as a "stabilization core" (Figures 4 and 5C), formed by four key stabilizing interactions that are highly conserved in nanobodies, unlike the human VH (Figures 5A and 5B). Interestingly, these four stabilizing residues are found on or next to loops (Figures 4 and 5C), which likely constrains the dynamics of these loops to in turn stabilize the overall nanobody structure—highlighting once again how the flexibility of loops on nanobodies influences their stability and consequently their antigen affinity. Our MD simulations further support this rationalization by suggesting that residue fluctuations in the FR3 region have a direct influence on CDR3 loop dynamics, which can then be modulated through FR3 re-engineering such as the point mutations we show. The strong conservation of the residues that form this stabilization core in all nanobodies, in contrast to antibody VH domains, suggests nanobodies have evolved to retain these integral stabilizing interactions—potentially as a substitute for the stabilizing effect of adjacent light chains found in conventional IgG antibodies. This nanobody feature allows guided optimization and tuning of nanobody affinity using only their primary sequence, as demonstrated by our affinity and stability enhancement of neutralizing nanobodies against SARS-CoV-2 with a single point mutation. Of note in the stability enhancement of our repertoire of SARS-CoV-2 nanobodies, is that all but one nanobody showed an improved or neutral effect on affinity upon introduction of the stabilizing mutations. The exception to this was the reengineering of the high-affinity binding S1-36, where introduction of the stabilizing interaction in an already high-affinity nanobody resulted in the S1-36 variant losing all detectable binding to its antigen. This exemplifies yet again the negative effect of *over-stabilizing* a nanobody. With the growing interest in utilizing nanobody technology[34–41] and particular emphasis placed on increasing nanobody stability, the results presented here suggest caution when optimizing nanobodies with the sole objective of increasing structural stability. We also present guidelines for the rational optimization of nanobodies through single point mutations within the FR3 region of nanobodies that can be applied readily to improve nanobody repertoires. We hope this study will aid researchers to rationally engineer their nanobody repertoires, including for use as diagnostics, prophylactics and therapeutics.

RESOURCE AVAILABILITY

Lead contact

Further information and requests for resources and reagents should be directed to and will be fulfilled by the lead contact, Michael P. Rout (rout@rockefeller.edu).

Materials availability

Plasmids generated in this study are available upon request by contacting the lead contact (rout@rockefeller.edu).

Data and code availability

All original code has been deposited https://github.com/tanmoy7989/nb_stability and is publicly available. X-ray diffraction data were collected at the X29A beamline (Brookhaven National Laboratory). The coordinates and structure factors of the X-ray crystal structures have been deposited in the Protein Data Bank with the accession codes PDB: 8SFS (LaG16:GFP); 8SLC (LaG43:GFP); 8G0I (LaG24:GFP); 8SFV (LaG19:GFP); 8SFX (LaG21:GFP); 8SG3 (LaG41:GFP); and 8SFZ (LaG35:GFP). Structures are publicly available. The accession codes are also listed in the key resources table. Any additional information required to reanalyze the data reported in this paper is available from the lead contact upon request.

ACKNOWLEDGMENTS

We would like to thank the Fisher Drug Discovery Resource Center (DDRC) (RRID:SCR_020985) at Rockefeller University, and especially former members Lavoisier Ramos-Espiritu and Carolina Adura for technical and data analysis support as well as the Rockefeller Structural Biology Resource Center (RRID: SCR_017732). We also thank members of the Rout, Almo and Chait labs for support and assistance. We acknowledge the support of the G. Harold and Leila Y. Mathers Charitable Foundation, the Robertson Therapeutic Development Fund, the Bay Area Lyme Foundation, the Jain Foundation, and the National Institutes of Health grants P41 GM109824 (M.P.R., B.T.C., and A.S.), R21 AI154180, U54 GM094662 (S.C.A.), U01 GM098256 (M.P.R. and A.S.), and R01 GM083960 (A.S.). Data was collected at NSLS beamline X29A that was funded by the Offices of Biological and Environmental Research and of Basic Energy Sciences of the US Department of Energy (P41 RR012408), and from the National Center for Research Resources of the National Institutes of Health (P41 GM103473).

AUTHOR CONTRIBUTIONS

Conceptualization, N.E.K. and M.P.R.; methodology, N.E.K. and T.S.; investigation, N.E.K., P.C.F., V.M., T.S., M.B., and M.K.T.; writing—original draft, N.E.K. and M.P.R.; writing—review and editing, N.E.K., P.C.F., V.M., T.S., M.B., M.K.T., D.A.O., A.S., B.T.C., J.B.B., and M.P.R.; funding acquisition, M.P.R., A.S., and S.C.A.; resources, M.P.R., A.S., and S.C.A.; supervision, M.P.R., A.S., and S.C.A.

DECLARATION OF INTERESTS

N.E.K., P.C.F., M.P.R., and B.T.C. are co-inventors on a provisional patent describing the anti-spike nanobodies described in this manuscript.

STAR★METHODS

Detailed methods are provided in the online version of this paper and include the following:

- KEY RESOURCES TABLE
- EXPERIMENTAL MODEL AND STUDY PARTICIPANT DETAILS
- METHOD DETAILS
  - Anti-GFP nanobody generation
  - Creating nanobody mutants
  - Protein expression and purification
  - Protein crystallization
  - Crystallographic data collection and processing
  - K_D determinations
  - Measurement of melting temperature (T_M)
  - Molecular modeling
- QUANTIFICATION AND STATISTICAL ANALYSIS

SUPPLEMENTAL INFORMATION

Supplemental information can be found online at https://doi.org/10.1016/j.str.2025.01.019.

Received: October 15, 2024
Revised: December 4, 2024
Accepted: January 16, 2025
Published: February 11, 2025

REFERENCES

1. Muyldermans, S. (2013). Nanobodies: natural single-domain antibodies. Annu. Rev. Biochem. *82*, 775–797. https://doi.org/10.1146/annurev-biochem-063011-092449.
2. Mast, F.D., Fridy, P.C., Ketaren, N.E., Wang, J., Jacobs, E.Y., Olivier, J.P., Sanyal, T., Molloy, K.R., Schmidt, F., Rutkowska, M., et al. (2021). Highly synergistic combinations of nanobodies that target SARS-CoV-2 and are resistant to escape. Elife *10*, e73027. https://doi.org/10.7554/eLife.73027.
3. De Genst, E., Silence, K., Decanniere, K., Conrath, K., Loris, R., Kinne, J., Muyldermans, S., and Wyns, L. (2006). Molecular basis for the preferential cleft recognition by dromedary heavy-chain antibodies. Proc. Natl. Acad. Sci. USA *103*, 4586–4591. https://doi.org/10.1073/pnas.0505379103.
4. Fridy, P.C., Li, Y., Keegan, S., Thompson, M.K., Nudelman, I., Scheid, J.F., Oeffinger, M., Nussenzweig, M.C., Fenyö, D., Chait, B.T., and Rout, M.P. (2014). A robust pipeline for rapid production of versatile nanobody repertoires. Nat. Methods *11*, 1253–1260.
5. Muyldermans, S. (2021). Applications of Nanobodies. Annu. Rev. Anim. Biosci. *9*, 401–421. https://doi.org/10.1146/annurev-animal-021419-083831.
6. Jovcevska, I., and Muyldermans, S. (2020). The Therapeutic Potential of Nanobodies. BioDrugs *34*, 11–26. https://doi.org/10.1007/s40259-019-00392-z.
7. Liu, M., Li, L., Jin, D., and Liu, Y. (2021). Nanobody-A versatile tool for cancer diagnosis and therapeutics. Wiley Interdiscip. Rev. Nanomed. Nanobiotechnol. *13*, e1697. https://doi.org/10.1002/wnan.1697.
8. Li, C., Zhan, W., Yang, Z., Tu, C., Hu, G., Zhang, X., Song, W., Du, S., Zhu, Y., Huang, K., et al. (2022). Broad neutralization of SARS-CoV-2 variants by an inhalable bispecific single-domain antibody. Cell *185*, 1389–1401.e18. https://doi.org/10.1016/j.cell.2022.03.009.
9. Pymm, P., Adair, A., Chan, L.J., Cooney, J.P., Mordant, F.L., Allison, C.C., Lopez, E., Haycroft, E.R., O'Neill, M.T., Tan, L.L., et al. (2021). Nanobody cocktails potently neutralize SARS-CoV-2 D614G N501Y variant and protect mice. Proc. Natl. Acad. Sci. USA *118*, e2101918118. https://doi.org/10.1073/pnas.2101918118.
10. Chi, X., Zhang, X., Pan, S., Yu, Y., Shi, Y., Lin, T., Duan, H., Liu, X., Chen, W., Yang, X., et al. (2022). An ultrapotent RBD-targeted biparatopic nanobody neutralizes broad SARS-CoV-2 variants. Signal Transduct. Targeted Ther. *7*, 44. https://doi.org/10.1038/s41392-022-00912-4.
11. Wu, X., Cheng, L., Fu, M., Huang, B., Zhu, L., Xu, S., Shi, H., Zhang, D., Yuan, H., Nawaz, W., et al. (2021). A potent bispecific nanobody protects hACE2 mice against SARS-CoV-2 infection via intranasal administration. Cell Rep. *37*, 109869. https://doi.org/10.1016/j.celrep.2021.109869.
12. Romao, E., Morales-Yanez, F., Hu, Y., Crauwels, M., De Pauw, P., Hassanzadeh, G.G., Devoogdt, N., Ackaert, C., Vincke, C., and Muyldermans, S. (2016). Identification of Useful Nanobodies by Phage Display of Immune Single Domain Libraries Derived from Camelid Heavy Chain Antibodies. Curr. Pharm. Des. *22*, 6500–6518. https://doi.org/10.2174/1381612822666160923114417.
13. Muyldermans, S., Baral, T.N., Retamozzo, V.C., De Baetselier, P., De Genst, E., Kinne, J., Leonhardt, H., Magez, S., Nguyen, V.K., Revets, H., et al. (2009). Camelid immunoglobulins and nanobody technology. Vet. Immunol. Immunopathol. *128*, 178–183.
14. Arbabi Ghahroudi, M., Desmyter, A., Wyns, L., Hamers, R., and Muyldermans, S. (1997). Selection and identification of single domain antibody fragments from camel heavy-chain antibodies. FEBS Lett. *414*, 521–526. https://doi.org/10.1016/s0014-5793(97)01062-4.
15. Saerens, D., Conrath, K., Govaert, J., and Muyldermans, S. (2008). Disulfide bond introduction for general stabilization of immunoglobulin heavy-chain variable domains. J. Mol. Biol. *377*, 478–488.

16. Vincke, C., Loris, R., Saerens, D., Martinez-Rodriguez, S., Muyldermans, S., and Conrath, K. (2009). General strategy to humanize a camelid single-domain antibody and identification of a universal humanized nanobody scaffold. J. Biol. Chem. *284*, 3273–3284.

17. Kunz, P., Zinner, K., Mücke, N., Bartoschik, T., Muyldermans, S., and Hoheisel, J.D. (2018). The structural basis of nanobody unfolding reversibility and thermoresistance. Sci. Rep. *8*, 7934. https://doi.org/10.1038/s41598-018-26338-z.

18. Govaert, J., Pellis, M., Deschacht, N., Vincke, C., Conrath, K., Muyldermans, S., and Saerens, D. (2012). Dual beneficial effect of interloop disulfide bond for single domain antibody fragments. J. Biol. Chem. *287*, 1970–1979. https://doi.org/10.1074/jbc.M111.242818.

19. Goldman, E.R., Liu, J.L., Zabetakis, D., and Anderson, G.P. (2017). Enhancing Stability of Camelid and Shark Single Domain Antibodies: An Overview. Front. Immunol. *8*, 865. https://doi.org/10.3389/fimmu.2017.00865.

20. Kunz, P., Ortale, A., Mucke, N., Zinner, K., and Hoheisel, J.D. (2019). Nanobody stability engineering by employing the DeltaTm shift; a comparison with apparent rate constants of heat-induced aggregation. Protein Eng. Des. Sel. *32*, 241–249. https://doi.org/10.1093/protein/gzz017.

21. Dingus, J.G., Tang, J.C.Y., Amamoto, R., Wallick, G.K., and Cepko, C.L. (2022). A general approach for stabilizing nanobodies for intracellular expression. Elife *11*, e68253. https://doi.org/10.7554/eLife.68253.

22. Kunz, P., Flock, T., Soler, N., Zaiss, M., Vincke, C., Sterckx, Y., Kastelic, D., Muyldermans, S., and Hoheisel, J.D. (2017). Exploiting sequence and stability information for directing nanobody stability engineering. Biochim. Biophys. Acta. Gen. Subj. *1861*, 2196–2205.

23. Cong, A.T.Q., Witter, T.L., and Schellenberg, M.J. (2022). High-efficiency recombinant protein purification using mCherry and YFP nanobody affinity matrices. Protein Sci. *31*, e4383. https://doi.org/10.1002/pro.4383.

24. Zhang, Z., Wang, Y., Ding, Y., and Hattori, M. (2020). Structure-based engineering of anti-GFP nanobody tandems as ultra-high-affinity reagents for purification. Sci. Rep. *10*, 6239. https://doi.org/10.1038/s41598-020-62606-7.

25. Mitchell, L.S., and Colwell, L.J. (2018). Comparative analysis of nanobody sequence and structure data. Proteins *86*, 697–706. https://doi.org/10.1002/prot.25497.

26. Zimmermann, I., Egloff, P., Hutter, C.A., Arnold, F.M., Stohler, P., Bocquet, N., Hug, M.N., Huber, S., Siegrist, M., Hetemann, L., et al. (2018). Synthetic single domain antibodies for the conformational trapping of membrane proteins. Elife *7*, e34317. https://doi.org/10.7554/eLife.34317.

27. Zavrtanik, U., Lukan, J., Loris, R., Lah, J., and Hadži, S. (2018). Structural Basis of Epitope Recognition by Heavy-Chain Camelid Antibodies. J. Mol. Biol. *430*, 4369–4386. https://doi.org/10.1016/j.jmb.2018.09.002.

28. Kazemi-Lomedasht, F., Muyldermans, S., Habibi-Anbouhi, M., and Behdani, M. (2018). Design of a humanized anti vascular endothelial growth factor nanobody and evaluation of its in vitro function. Iran. J. Basic Med. Sci. *21*, 260–266. https://doi.org/10.22038/ijbms.2018.24898.6183.

29. Moutel, S., Bery, N., Bernard, V., Keller, L., Lemesre, E., de Marco, A., Ligat, L., Rain, J.C., Favre, G., Olichon, A., and Perez, F. (2016). NaLi-H1: A universal synthetic library of humanized nanobodies providing highly functional antibodies and intrabodies. Elife *5*, e16228. https://doi.org/10.7554/eLife.16228.

30. Soler, M.A., Medagli, B., Wang, J., Oloketuyi, S., Bajc, G., Huang, H., Fortuna, S., and de Marco, A. (2021). Effect of Humanizing Mutations on the Stability of the Llama Single-Domain Variable Region. Biomolecules *11*, 163. https://doi.org/10.3390/biom11020163.

31. Krissinel, E., and Henrick, K. (2007). Inference of macromolecular assemblies from crystalline state. J. Mol. Biol. *372*, 774–797.

32. Lange, O.F., and Grubmüller, H. (2006). Generalized correlation for biomolecular dynamics. Proteins *62*, 1053–1061. https://doi.org/10.1002/prot.20784.

33. Bond, C.J., Marsters, J.C., and Sidhu, S.S. (2003). Contributions of CDR3 to V H H domain stability and the design of monobody scaffolds for naive antibody libraries. J. Mol. Biol. *332*, 643–655. https://doi.org/10.1016/s0022-2836(03)00967-7.

34. Bao, C., Gao, Q., Li, L.L., Han, L., Zhang, B., Ding, Y., Song, Z., Zhang, R., Zhang, J., and Wu, X.H. (2021). The Application of Nanobody in CAR-T Therapy. Biomolecules *11*, 238. https://doi.org/10.3390/biom11020238.

35. Bao, G., Tang, M., Zhao, J., and Zhu, X. (2021). Nanobody: a promising toolkit for molecular imaging and disease therapy. EJNMMI Res. *11*, 6. https://doi.org/10.1186/s13550-021-00750-5.

36. Deken, M.M., Kijanka, M.M., Beltrán Hernández, I., Slooter, M.D., de Bruijn, H.S., van Diest, P.J., van Bergen En Henegouwen, P.M.P., Lowik, C.W.G.M., Robinson, D.J., Vahrmeijer, A.L., and Oliveira, S. (2020). Nanobody-targeted photodynamic therapy induces significant tumor regression of trastuzumab-resistant HER2-positive breast cancer, after a single treatment session. J. Control. Release *323*, 269–281. https://doi.org/10.1016/j.jconrel.2020.04.030.

37. Marable, J., Ruiz, D., Jaiswal, A.K., Bhattacharya, R., Pantazes, R., Agarwal, P., Suryawanshi, A.S., Bedi, D., Mishra, A., Smith, B.F., and Sandey, M. (2021). Nanobody-based CTLA4 inhibitors for immune checkpoint blockade therapy of canine cancer patients. Sci. Rep. *11*, 20763. https://doi.org/10.1038/s41598-021-00325-3.

38. Martinez-Delgado, G. (2020). Inhaled nanobodies against COVID-19. Nat. Rev. Immunol. *20*, 593. https://doi.org/10.1038/s41577-020-00443-5.

39. Messer, A., and Butler, D.C. (2020). Optimizing intracellular antibodies (intrabodies/nanobodies) to treat neurodegenerative disorders. Neurobiol. Dis. *134*, 104619. https://doi.org/10.1016/j.nbd.2019.104619.

40. Wouters, Y., Jaspers, T., Rué, L., Serneels, L., De Strooper, B., and Dewilde, M. (2022). VHHs as tools for therapeutic protein delivery to the central nervous system. Fluids Barriers CNS *19*, 79. https://doi.org/10.1186/s12987-022-00374-4.

41. Yang, E.Y., and Shah, K. (2020). Nanobodies: Next Generation of Cancer Diagnostics and Therapeutics. Front. Oncol. *10*, 1182. https://doi.org/10.3389/fonc.2020.01182.

42. Meng, E.C., Goddard, T.D., Pettersen, E.F., Couch, G.S., Pearson, Z.J., Morris, J.H., and Ferrin, T.E. (2023). UCSF ChimeraX: Tools for structure building and analysis. Protein Sci. *32*, e4792. https://doi.org/10.1002/pro.4792.

43. Otwinowski, Z., and Minor, W. (1997). Processing of X-ray diffraction data. Methods Enzymol. *276*, 307–326.

44. Winn, M.D., Ballard, C.C., Cowtan, K.D., Dodson, E.J., Emsley, P., Evans, P.R., Keegan, R.M., Krissinel, E.B., Leslie, A.G.W., McCoy, A., et al. (2011). Overview of the CCP4 suite and current developments. Acta Crystallogr. D Biol. Crystallogr. *67*, 235–242.

45. McCoy, A.J., Grosse-Kunstleve, R.W., Adams, P.D., Winn, M.D., Storoni, L.C., and Read, R.J. (2007). Phaser crystallographic software. J. Appl. Crystallogr. *40*, 658–674.

46. Emsley, P., and Cowtan, K. (2004). Coot: model-building tools for molecular graphics. Acta Crystallogr. D Biol. Crystallogr. *60*, 2126–2132.

47. Liebschner, D., Afonine, P.V., Baker, M.L., Bunkóczi, G., Chen, V.B., Croll, T.I., Hintze, B., Hung, L.W., Jain, S., McCoy, A.J., et al. (2019). Macromolecular structure determination using X-rays, neutrons and electrons: recent developments in Phenix. Acta Crystallogr. D Struct. Biol. *75*, 861–877. https://doi.org/10.1107/S2059798319011471.

48. Laskowski, R.A., MacArthur, M.W., Moss, D.S., and Thornton, J.M. (1993). PROCHECK: a program to check the stereochemical quality of protein structures. J. Appl. Crystallogr. *26*, 283–291.

49. Eastman, P., Swails, J., Chodera, J.D., McGibbon, R.T., Zhao, Y., Beauchamp, K.A., Wang, L.P., Simmonett, A.C., Harrigan, M.P., Stern, C.D., et al. (2017). OpenMM 7: Rapid development of high performance algorithms for molecular dynamics. PLoS Comput. Biol. *13*, e1005659. https://doi.org/10.1371/journal.pcbi.1005659.

50. Maier, J.A., Martinez, C., Kasavajhala, K., Wickstrom, L., Hauser, K.E., and Simmerling, C. (2015). ff14SB: Improving the Accuracy of Protein Side Chain and Backbone Parameters from ff99SB. J. Chem. Theory Comput. *11*, 3696–3713. https://doi.org/10.1021/acs.jctc.5b00255.

51. Jorgensen, W.L., Chandrasekhar, J., Madura, J.D., Impey, R.W., and Klein, M.L. (1983). Comparison of simple potential functions for simulating liquid water. J. Chem. Phys. *79*, 926–935.

52. Mandell, D.J., Coutsias, E.A., and Kortemme, T. (2009). Sub-angstrom accuracy in protein loop reconstruction by robotics-inspired conformational sampling. Nat. Methods *6*, 551–552. https://doi.org/10.1038/nmeth0809-551.

53. McGibbon, R.T., Beauchamp, K.A., Harrigan, M.P., Klein, C., Swails, J.M., Hernández, C.X., Schwantes, C.R., Wang, L.P., Lane, T.J., and Pande, V.S. (2015). MDTraj: A Modern Open Library for the Analysis of Molecular Dynamics Trajectories. Biophys. J. *109*, 1528–1532. https://doi.org/10.1016/j.bpj.2015.08.015.

Please cite this article in press as: Ketaren et al., Unique mechanisms to increase structural stability and enhance antigen binding in nanobodies, Structure (2025), https://doi.org/10.1016/j.str.2025.01.019

STAR★METHODS

KEY RESOURCES TABLE

REAGENT or RESOURCE	SOURCE	IDENTIFIER
Bacterial and virus strains		
ArcticExpress (DE3) cells	Agilent	Cat#230192
E. coli XL10-Gold Ultracompetent cells	Agilent	Cat#200315
E. coli BL21-Gold (DE3) cells	Agilent	Cat#230132
Chemicals, peptides, and recombinant proteins		
HEPES	Fisher Scientific	Cat#BP310-1
NaCl	Fisher Scientific	Cat# S271-3
Tween 20	Fisher Scientific	Cat# BP337-500
10 mM Na acetate pH 4.5	Bio Rad	Cat#1762121
Magnesium chloride hexahydrate	Sigma-Aldrich	Cat#M9272-500G
Imidazole, ReagentPlus®, 99%	Sigma-Aldrich	Cat#I202-500G
PBS, 10x, pH 7.4	Thermo-Scientific	Cat#J62036-K3
Tris-base	Fisher Scientific	Cat#BP152-1
Sucrose	Fisher Scientific	Cat#BP220-212
EDTA	Fisher Scientific	Cat# BP120-1
Glycine	Sigma	Cat#G7126-5kg
BamHI-HF	NEB	Cat#R3136S
XhoI	NEB	Cat#R0146S
T4 DNA ligase	NEB	Cat#M0202S
SYPRO® Orange Protein Gel Stain	Millipore-Sigma	Cat# S5692-500UL
LaG16	Fridy et al.[4]	N/A
LaG19	Fridy et al.[4]	N/A
LaG21	Fridy et al.[4]	N/A
LaG24	Fridy et al.[4]	N/A
LaG35	Fridy et al.[4]	N/A
LaG41	Fridy et al.[4]	N/A
LaG43	Fridy et al.[4]	N/A
$LaG43_{N78R}$	This paper	N/A
$LaG43_{K80R}$	This paper	N/A
$LaG43_{N81R}$	This paper	N/A
$LaG19_{S102R}$	This paper	N/A
$LaG19_{Q103V}$	This paper	N/A
$LaG19Q_{103I}$	This paper	N/A
$LaG21_{L69F}$	This paper	N/A
$LaG16_{E91K}$	This paper	N/A
$LaG24_{Q68K}$	This paper	N/A
$LaG24_{H85Q}$	This paper	N/A
S1-8	Mast et al.	N/A
$S1\text{-}8_{L70F}$	This paper	N/A
S1-28	Mast et al.[2]	N/A
$S1\text{-}28_{L70F}$	This paper	N/A
S1-36	Mast et al.[2]	N/A
$S1\text{-}36_{L70F}$	This paper	N/A
S1-40	Mast et al.[2]	N/A

(*Continued on next page*)

Please cite this article in press as: Ketaren et al., Unique mechanisms to increase structural stability and enhance antigen binding in nanobodies, Structure (2025), https://doi.org/10.1016/j.str.2025.01.019

Continued

REAGENT or RESOURCE	SOURCE	IDENTIFIER
S1-40$_{S89K}$	This paper	N/A
S1-RBD-14	Mast et al.[2]	N/A
S1-RBD-14$_{E89K}$	This paper	N/A
S1-RBD-42	Mast et al.[2]	N/A
S1-RBD-42$_{E88K}$	This paper	N/A
S1-14	Mast et al.[2]	N/A
S1-14$_{Q66K}$	This paper	N/A
S1-RBD-31	Mast et al.[2]	N/A
S1-RBD-31$_{Q67K}$	This paper	N/A
Deposited data		
LaG16:GFP complex	This paper	PDB ID: 8SFS
LaG43:GFP complex	This paper	PDB ID: 8SLC
LaG24:GFP complex	This paper	PDB ID: 8G0I
LaG19:GFP complex	This paper	PDB ID: 8SFV
LaG21:GFP complex	This paper	PDB ID: 8SFX
LaG41:GFP complex	This paper	PDB ID: 8SG3
LaG35:GFP complex	This paper	PDB ID: 8SFZ
Critical commercial assays		
ProteOn Amine Coupling Kit	Bio-Rad	Cat#1762410
Amine Coupling Kit	Cytiva	Cat#BR100050
MCSG-1 crystallization screen	Molecular dimensions	Cat# MCSG-1
MCSG-2 crystallization screen	Molecular dimensions	Cat# MCSG-2
MCSG-4 crystallization screen	Molecular dimensions	Cat# MCSG-4
Recombinant DNA		
pET21-pelB	Fridy et al.[4]	N/A
Software and algorithms		
UCSF ChimeraX	Meng et al.[42]	https://www.rbvi.ucsf.edu/chimerax/download.html
HKL3000	Otwinowski et al.[43]	https://www.hkl-xray.com/hkl-3000
COOT	Emsley and Cowtan[46]	https://www2.mrc-lmb.cam.ac.uk/personal/pemsley/coot/
PHENIX	Liebschner et al.[47]	https://phenix-online.org/
CCP4 software suit (incudes Mosflm, Phaser, Scala, Procheck)	Winn et al.[44]	https://www.ccp4.ac.uk
PyMOL	Schrodinger, LLC	https://pymol.org/
ProteOn Manager software	Bio-Rad	N/A
Biacore Insight Evaluation software	Cytiva	Cat#29310602
openMM molecular simulation toolkit	Eastman et al.[49]	https://openmm.org/
pyRosetta	Mandell et al.[52]	https://www.pyrosetta.org/
mdtraj Python package	McGibbon et al.[53]	https://www.mdtraj.org/1.9.8.dev0/index.html
Other		
ProteOn GLC Sensor Chip	Bio-Rad	Cat#176-5011
Series S Sensor Chip CM5	Cytiva	Cat#BR100530
Hard-shell PCR plates, 96 well, thin-wall	Bio-Rad	Cat#HSP9661
96-well INTELLI-plates	Art Robbins Instruments,	Cat#MAR-102-0011-00
TALON® Metal Affinity Resin	Takara Bio	Cat# 635504
Superdex 75 10/300 GL size-exclusion column	Cytiva	Cat#17517401
Microseal 'B' Adhesive Seals MSB1001BEDU	Bio-Rad	Cat# MSB1001

Please cite this article in press as: Ketaren et al., Unique mechanisms to increase structural stability and enhance antigen binding in nanobodies, Structure (2025), https://doi.org/10.1016/j.str.2025.01.019

EXPERIMENTAL MODEL AND STUDY PARTICIPANT DETAILS

Nanobodies generated in this study are from two previous studies.[2,4] Llama care was performed at Capralogics, Inc. in compliance with the protocols approved by their Institutional Care and Use Committee (IACUC). The bacterial strains *E. coli* XL10-Gold Ultracompetent cells and *E. coli* ArcticExpress (DE3) cells were used for propagation of plasmid DNA and protein expression respectively. *E. coli* BL21-Gold (DE3) cells were used for expression of recombinant GFP and GFP variants.

METHOD DETAILS

Anti-GFP nanobody generation

Anti-GFP nanobodies were generated as previously described.[4] In brief, we immunized a llama with GFP. After a strong immune response was elicited, we collected lymphocytes from bone marrow, highly enriched for active B cells. We then purified RNA from these cells and performed high-throughput sequencing on the PCR-amplified variable region (VHH) of heavy-chain-only IgG variants (HCAbs). In parallel, we collected animal sera, and affinity purified HCAbs with strong affinity and specificity to each antigen. The purified HCAbs were then proteolytically cleaved to generate the antigen-binding VHH fragments, which we analyzed by bottom-up Mass spectrometry (MS). Correlating peptides to the DNA database of full-length sequences using customized Llama-Magic software, we identified candidate nanobody clones. Codon-optimized genes for these clones were synthesized and cloned into a pET21-pelB *E. coli* periplasmic expression vector and expressed in *E. coli* Arctic Express (DE3) cells (Agilent); cell lysates were passed over an antigen-conjugated resin to screen for positive nanobodies.

Creating nanobody mutants

Nanobody mutants were created by synthesizing genes with desired substitutions as gBlocks from Integrated DNA Technologies (www.idtdna.com). The gblocks (IDT) are cloned into a peT21b vector via a C-terminal BamHI and N-terminal XhoI restriction sites using T4 DNA Ligase (NEB) using the manufacturers guidelines and correct insertions confirmed via Sanger sequencing. All mutant nanobody protein sequences are found in Tables S5–S7.

Protein expression and purification

Protein expression and purification was performed as described previously.[4] Briefly, periplasmic expression constructs carrying the His-tagged nanobody variants were individually expressed in *E. coli* Arctic Express (DE3) cells (Agilent) and pellets resuspended in TES buffer (200mM Tris-HCl, pH 8.0, 0.5mM EDTA, pH 8.0, 500mM Sucrose), periplasmic fractions released via osmotic shock in TES diluted 1 in 4 with ddH_2O. Samples were then spun at 25,000 rpm for 20 minutes at 4°C. Supernatant was retained, 5 M NaCl was added to make a final concentration of 0.15 M and then passed over a TALON® Metal Affinity Resin (Takara Bio) (800 uL of TALON® Metal Affinity Resin was used per liter of starting expression culture) equilibrated with 20mM Na-HEPES, pH 8.0, 150mM NaCl. Resin was washed with wash buffer 1 (20mM Na-HEPES, pH 8.0, 900mM NaCl) followed by wash buffer 2 (20mM Na-HEPES, pH 8.0, 150mM NaCl, 10mM imidazole, pH 8.0). Protein was eluted with 20mM Na-HEPES, pH 8.0, 150mM NaCl, 250mM imidazole, pH 8.0), collecting 1 mL fractions. Purified protein was then dialysed in 20mM Na-HEPES, pH 8.0, 150mM NaCl. To prepare GFP complexes for crystallization, untagged GFP was expressed in *E. coli* BL21-Gold (DE3) cells (Agilent), which were lysed using a microfluidizer. Before elution, nanobody protein captured on TALON® Metal Affinity resin, was incubated with a saturating amount of GFP in cell lysate, washed with wash buffer 2, and the GFP-nanobody complex eluted using imidazole. Eluted protein was passed over a Superdex 75 10/300 GL size-exclusion column (Cytiva) in PBS. Purity of protein preparations was analyzed via SDS-PAGE, and concentrations determined by UV absorbance. Samples for crystallography were concentrated by ultrafiltration when necessary.

Protein crystallization

Concentrations of each nanobody-GFP complex were as follows: LaG16, 10 mg mL^{-1}; LaG19, 16 mg ml^{-1}; LaG21, 17 mg mL^{-1}; LaG24, 11 mg mL^{-1}; LaG35, 13 mg mL^{-1}; LaG41, 10 mg mL^{-1}; LaG43, 15 mg mL^{-1}. GFP- nanobody complexes at a 1:1 ratio of protein complex to reservoir buffer were crystallized via the sitting-drop vapor diffusion method where the protein solutions (0.3uL) were mixed with an equal volume of a precipitant solution and equilibrated at room temperature (294 K) against the same precipitant solution in clear tape-sealed 96-well INTELLI-plates (Art Robbins Instruments, Sunnyvale, CA) and incubated at 18°C. Proteins were screened against the commercial screens MCSG1, MCSG2, and MCSG4 (Molecular dimensions). Crystallization was performed using either a TECAN crystallization robot (TECAN US, Research Triangle Park, NC) or a PHOENIX crystallization robot (Art Robbins Instruments). The following reservoir conditions produced crystals for subsequent data collection: LaG16-GFP complex, 0.1 M HEPES pH 7.5, 1.26 M ammonium sulphate; LaG19-GFP complex, 0.2 M lithium sulphate, 0.1 M tris pH 7.0, 1 M potassium sodium tartrate; LaG21-GFP complex, 1 M bis-tris propane pH 7.0, 1.2 M DL-malic acid pH 7.0; LaG24-GFP complex, 0.2 M potassium chloride, 20% (w/v) PEG3350; LaG35-GFP complex, 0.2 M potassium formate pH 7.3, 20% (w/v) PEG3350; LaG41-GFP, 0.2 M sodium potassium phosphate pH 6.2, 2.5 M sodium chloride; LaG43-GFP, 0.1 M sodium acetate pH 4.6, 2 M sodium formate. The crystals were harvested using cryogenic loops, cryoprotected using 20% glycerol and flash cooled in liquid nitrogen.

Please cite this article in press as: Ketaren et al., Unique mechanisms to increase structural stability and enhance antigen binding in nanobodies, Structure (2025), https://doi.org/10.1016/j.str.2025.01.019

Crystallographic data collection and processing

X-ray diffraction data was collected at the X29A beamline (Brookhaven National Laboratory) at a wavelength of 1.075 Å. All data were indexed, integrated and scaled with HKL3000.[43] The X-diffraction data for the LaG21-GFP complex was collected on the 31-ID beamline (Advanced Photon Source) at a wavelength of 0.9793 Å and data was indexed, integrated using MOSFLM and scaled using SCALA using the CCP4 software suit.[44] All structures were determined using molecular replacement with PHASER[45] using as input models the GFP structure (1EMA) and the nanobody (4KRN). Each dataset underwent multiple cycles of manual editing and adjustment of the model using COOTv0.9.8.6.[46] Refinement was performed in PHENIXv1.19.2-4158.[47] The final models were validated with PROCHECK,[48] PDBePISA[31] and images created using PyMOL (Schrodinger LLC 2015). Data collection and statistics are summarized in Table 1.

K_D determinations

K_D's were determined via surface plasmon resonance experiments. Measurements were either taken on a Proteon XPR36 Protein Interaction Array System (Bio-Rad) or a Biacore 8k (Cytiva) at 25°C. Recombinant GFP was immobilized on a ProteOn GLC sensor chip as previously described.[4] using the ProteOn Amine Coupling Kit (EDC/NHS coupling chemistry, Bio-Rad) according to the respective manufacturer's guidelines either on a ProteOn GLC sensor chip or a Series S CM5 sensor chip. All purified nanobodies in a final buffer containing 20 mM HEPES pH 7.4, 150 mM NaCl, 0.02% Tween, were prepared in 5–8 concentrations. For experiments performed on the Proteon XPR36, protein was then injected at 50 μl/min for 120 s, followed by a dissociation time of 600 s. Residual bound proteins were removed by regenerating the chip surface using glycine pH 3, 1 M $MgCl_2$. Data were processed and analyzed using the ProteOn Manager software. For experiments performed on the Biacore 8k, protein was injected at 60 μl/min for 120 s, followed by a dissociation time of either 1200 s or 2400s. Residual bound proteins were removed by regenerating the chip surface using 1 M $MgCl_2$. Data were processed and analyzed using the Biacore Insight Evaluation software.

Measurement of melting temperature (T_M)

The melting temperature (T_M) of the anti-GFP nanobody variants was measured by differential scanning fluorimetry (DSF) using a CFX96 Real Time PCR Detection System (Bio-Rad, Hercules, CA). A 96-well thin-wall PCR plate (Bio-Rad) was set up with each well containing 10-20 μM protein samples, 5 × SYPRO Orange dye (Millipore-Sigma), 20 mM HEPES, 150 mM NaCl buffer (pH 7.5). The assay measured a fluorescence variation over a temperature range of 25–95°C that was increased at a rate of 0.5°C/30 s. The excitation and emission wavelengths were 490 and 575 nm respectively. T_M was the transition midpoint value between the start point and the maximum point, which was calculated using the manufacturer's software.

Molecular modeling

Molecular dynamics (MD) simulations of solvated wildtype and mutated (L69F) LaG-21 were implemented with the openMM molecular simulation toolkit,[49] using the ff14SB amber forcefield[50] for the protein, and a tip3p water model.[51] All simulations used a nonbonded cutoff of 10 Å, hydrogen mass of 4 amu, and timestep of 2 fs. To study the effect of temperature, we performed separate simulations at 300, 336 and 421 K. For each temperature, 8 independent copies of the system were simulated starting from slightly different initial conformations of the CDR-H3 loop (IMGT-based numbering) generated using a single iteration of the KicMover protocol, followed by 5 iterations of the FastRelax protocol in pyRosetta.[52] In each copy, the LaG21 crystal structure was first solvated using openMM's automatic solvation routine, and then relaxed under NPT conditions at 1.013 bar pressure and 300 K temperature: first for 4 ns with 1 kcal/$Å^2$ position restraints on all protein atoms, followed by further 2 ns of unrestrained simulation. The last 400 ps from the unrestrained NPT round was used to estimate the average dimensions of the cubical box required to maintain the expected water density (in the tip3p model) at 1.013 bar and 300 K. A second round of simulations was then performed under NVT conditions using the calculated box length, where the system was slowly annealed over 10 ns starting from 300 K and extending over a range of 10 exponentially distributed temperatures until the desired temperature was reached. Ultimately, an additional 100 ns of production runs under NVT conditions were carried out at the desired temperature and trajectory snapshots were recorded every 20 ps. Thus, we ran a total of 1.6 μs of production MD at each temperature, out of which the last 400 ns were used for collecting statistics. Average root mean square fluctuations of residues and backbone dihedral angles were calculated with the mdtraj Python package.[53] Overall deviation of nanobody backbone dihedral angles (ϕ,ψ) from the reference crystal structure (ϕ_{ref},ψ_{ref}) was calculated for the i^{th} residue as $\Delta^i_{\phi\psi} = \sqrt{(\phi^i - \phi^i_{ref})^2+(\psi^i - \psi^i_{ref})^2}$ at every trajectory frame. We calculated the self (H_i, H_j) and pairwise (H_{ij}) Gibbs entropies of the system along the backbone dihedral deviation order parameter as:

$$H_i = -\sum p\left(\Delta^i_{\phi\psi}\right) log\, p\left(\Delta^i_{\phi\psi}\right) \text{ and,}$$

$$H_{ij} = -\sum p\left(\Delta^i_{\phi\psi}, \Delta^j_{\phi\psi}\right) log\, p\left(\Delta^i_{\phi\psi}, \Delta^j_{\phi\psi}\right)$$

where $p(x)$ is the probability distribution of the order parameter x (here, $\Delta_{\phi\psi}$) and is calculated by histogramming the dihedral deviation data from the simulation, while the summation is carried out over all trajectory frames. Subsequently, the mutual information (M_{ij})

Please cite this article in press as: Ketaren et al., Unique mechanisms to increase structural stability and enhance antigen binding in nanobodies, Structure (2025), https://doi.org/10.1016/j.str.2025.01.019

between residues *i* and *j* was calculated as[32] $M_{ij} = H_i + H_j - H_{ij}$ and normalized to a generalized correlation coefficient between 0 and 1 as $C_{ij} = \sqrt{1 - exp\left(-\frac{2M_{ij}}{3}\right)}$.

QUANTIFICATION AND STATISTICAL ANALYSIS

For molecular modeling, uncertainties of RMS fluctuations at each temperature in Figure 6A (shaded profiles around the mean trend denoted by circular markers) were calculated by first dividing the per-residue RMS fluctuation data from the MD simulation trajectory into n = 4 blocks, and then reporting the standard deviation around the mean from these blocks. Per-residue RMS fluctuation data between these blocks were confirmed to be de-correlated by computing the auto-correlation coefficient between data-points from all pairs of blocks, and averaging over the total block size and number of residues. Mutual Information (MI) between pairs of residues in Figure S10, were computed similarly by dividing the data into n = 4 blocks, and reporting the mean MI. The standard deviation in MI values between these independent blocks were not reported in Figure S10, and they are of the order of ~3.2% of the mean MI. All calculations were done using the NumPy package (version 1.26.0) of the Python programming language (version 3.10.5). X-ray crystallography data collection and refinement statistics are summarized in Table 1.